Inorganic Chemistry

pubs.acs.org/IC Article

# Deep-Red-Fluorescent Zinc Probe with a Membrane-Targeting Cholesterol Unit

Jin Ju Kim,[†] Jayeon Hong,[†] Seungyeon Yu, and Youngmin You*

Cite This: https://dx.doi.org/10.1021/acs.inorgchem.0c01376 Read Online

ACCESS | Metrics & More | Article Recommendations | Supporting Information

**ABSTRACT:** Organelle-targeting fluorescence probes are valuable because they can provide spatiotemporal information about the trafficking of analytes of interest. The spatiotemporal resolution can be improved by using low-energy emission signals because they are barely contaminated by autofluorescence noises. In this study, we designed and synthesized a deep-red-fluorescent zinc probe (JJ) with a membrane-targeting cholesterol unit. This zinc probe consists of a boron-azadipyrromethene (aza-BODIPY) fluorophore and a zinc receptor that is tethered to a tri(ethylene glycol)−cholesterol chain. In aqueous solutions buffered to pH 7.4, JJ exhibits weak fluorescence with a peak wavelength of 663 nm upon excitation at 622 nm. The addition of $ZnCl_2$ elicits an approximately 5-fold enhancement of the fluorescence emission with a fluorescence dynamic range of 141000. Our electrochemical and picosecond transient photoluminescence investigations indicate that the fluorescence turn-on response is due to the zinc-induced abrogation of the formation of a nonemissive intramolecularly charge-separated species, which occurs with a driving force of 0.98 eV. The fluorescence zinc response was found to be fully reversible and to be unaffected by pH changes or the presence of biological metal ions. These properties are due to tight zinc binding with a dissociation constant of 4 pM. JJ was found to be nontoxic to HeLa cells up to submicromolar concentrations, which enables cellular imaging. Colocalization experiments were performed with organelle-specific stains and revealed that JJ is rapidly internalized into intracellular organelles, including lysosomes and endoplasmic reticula. Unexpectedly, probe internalization was found to permeabilize the cell membrane, which facilitates the influx of exogens such as zinc ions. Such permeabilization does not arise for a control probe without the tri(ethylene glycol)−cholesterol chain (JJC). Our results show that the membrane-targeting cholesterol unit can disrupt membrane integrity.

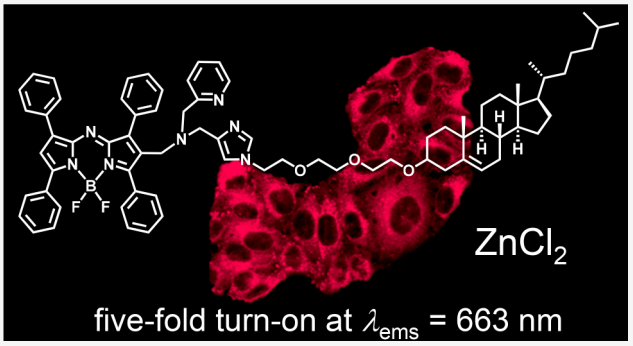


## INTRODUCTION

The human body contains a pool of free, mobile zinc.[1−4] Intracellular levels of mobile zinc are tightly regulated between the picomolar and micromolar concentrations by the actions of metallothionein and the systems involving zinc-transporter proteins.[1,5−7] Failures in zinc homeostasis are intimately linked to the genesis and development of pathological conditions.[8−23] Growing evidence also indicates that free zinc mediates physiological actions, including immune and brain function,[24−33] gene transcription,[34,35] apoptosis regulation,[36−38] mammalian reproduction,[39,40] and redox modulation.[41] These findings are part of a general consensus that the knowledge of zinc biochemistry can provide useful insights into the development of theranostic tools.

The study of zinc biology requires fundamental information about the location, concentration, and trafficking of free zinc. However, the $d^{10}$ electronic configuration of $Zn^{2+}$ precludes the use of the multifarious spectroscopic techniques available for the study of biological transition metals. Fluorescent probe techniques have been the most successful for the study of free zinc, as they are compatible with live specimens and afford zinc-induced fluorescence responses with high spatiotemporal resolution and large dynamic ranges.[42−55]

One promising strategy for maximizing the sensing capability of zinc probes is their targeted delivery at specific locations. Probe localization prevents the alteration of zinc homeostasis in probe-free regions. The use of localizable zinc probes also minimizes fluorescence artifacts due to environmental effects such as pH and viscosity that vary over the range of intracellular organelles. A particular advantage of localizable zinc probes is the improved spatial resolution of zinc-releasing events within the region of interest.

Previous research has established a library of organelle-specific probes capable of reporting zinc in mitochondria,[56−60]

Received: May 11, 2020

Downloaded via UNIV OF GOTHENBURG on July 28, 2020 at 12:48:48 (UTC).
See https://pubs.acs.org/sharingguidelines for options on how to legitimately share published articles.


© XXXX American Chemical Society

https://dx.doi.org/10.1021/acs.inorgchem.0c01376
Inorg. Chem. XXXX, XXX, XXX−XXX

lysosomes,[60−64] endoplasmic reticula,[60,65,66] and the Golgi apparatus.[67,68] It is anticipated that combinations of these probes will aid the research into intracellular zinc signaling between organelles. Cell-membrane-targeting zinc probes have a particular advantage in this area.[69] Probes anchored to the outer surface of the plasma membrane can monitor intercellular zinc signaling between cells. In a central example of such techniques, the fluorescence detection of synaptic transmission that is mediated by the efflux of vesicular zinc from presynaptic neurons has been reported.[70] In addition, the secretion of insulin can be traced by attaching fluorescence zinc probes to the plasma membranes of pancreatic cells.[71] These examples demonstrate the particular utility of membrane-targeting zinc probes.

The majority of membrane-targetable zinc probes contain alkyl moieties. The hydrophobic interactions of these moieties with lipids result in the adhesion of the probe to the extracellular surfaces of the plasma membranes of cells. Li and co-workers pioneered this design strategy by adding two dodecyl chains to fluorescein that possessed a zinc receptor at its bottom ring.[71] This zinc probe can be used to monitor the exocytotic release of pancreatic zinc upon depolarization with KCl. Similar strategies have recently been pursued by the groups of Lippard and Xu.[72,73] Watkinson and co-workers explored synthetic approaches to creating membrane-targeting zinc probes.[60,74] A membrane-targetable, two-photon-excitable fluorescence probe has also been fabricated through the addition a nonyl chain.[75] As an alternative to simple alkyl chains, cholesterol has been found to facilitate the localization of fluorescence probes on the outer membranes of cells. Taki and co-workers demonstrated the fluorescence visualization of extracellular zinc by using a fluorescein-based zinc probe with appended cholesterol.[76] The Li group recently extended this strategy by replacing the hydrophobic units with a HaloTag substrate. This genetically encoded zinc probe was found to be capable of the visualization of secretory granular zinc in pancreatic islet $\beta$ cells.[77] In a later study, the Li group further modified the probe with truncated exendin-4, which binds strongly with the glucagon-like peptide 1 receptors present on the surfaces of $\beta$ cells.[78] An earlier study by Palmer and co-workers revealed the membrane localization of a dyad containing a cyan fluorescent protein (CFP) and a yellow fluorescent protein (YFP) linked through a $His_4$ motif.[79]

As outlined above, the design to date of membrane-localizable probes has mainly focused on the targeting moieties. The choice of fluorogenic scaffolds remains narrow; only blue- or green-fluorescent platforms, including fluorescein,[71,72,76−78] naphthyldiimide,[60,73,74] and quinaldine,[72] have been demonstrated. Obviously, these fluorophores are not perfect for bioimaging as they rely on relatively high-energy excitation beams. Although the use of two-photon excitable fluorescence reduces the photocytotoxicity,[75] its applications are limited because of the requirement of sophisticated laser optics. These limitations indicate that zinc probes must exhibit low-energy fluorescence emission upon single-photon excitation.

Herein, we report the design, synthesis, and zinc-sensing applications of a deep-red-fluorescent probe tethered to a membrane-targeting cholesterol unit (JJ, Figure 1). Cholesterol interacts strongly with the plasma membrane of mammalian cells, due to its high rigidity and lipophilicity. The unique membrane anchoring ability was exploited to create membrane-localizable probes of copper and zinc.[76,80] JJ exhibits a 5-fold fluorescence turn-on response to zinc ions with a peak emission wavelength of 663 nm under photoexcitation at 622 nm in aqueous buffers. Our spectroscopic and electrochemical results indicate that the fluorescence turn-on signaling is mediated by the zinc-induced abrogation of the photoinduced one-electron transfer, which occurs with a driving force as large as 0.98 eV even for a narrow bandgap energy (1.87 eV). This fluorescence zinc signaling is not affected by changes in pH or the presence of biological metal ions. JJ binds zinc tightly with a zinc dissociation constant of 4 pM, which ensures high zinc selectivity. The bioimaging utility was demonstrated by treating HeLa cells with our probe. Our fluorescence microscopic experiments show that JJ is promptly internalized into intracellular regions while the cells remain live. Unexpectedly, we found that this probe internalization permeabilizes the cell membrane, which facilitates the entry of extracellular zinc without the need for a pyrithione ionophore.

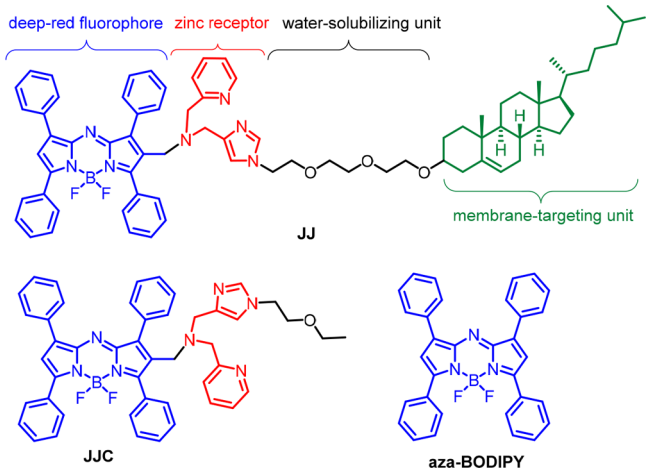


**Figure 1.** Chemical structures of the fluorescence zinc probe (JJ) and its control molecules (JJC and aza-BODIPY).

## RESULTS AND DISCUSSION

**Design and Syntheses.** Figure 1 depicts the chemical structures of JJ and its control compounds. Aza-BODIPY was chosen as a fluorescent scaffold because of its outstanding emission properties in the deep-red emission region.[81] An *N*-(4-imidazolyl)-*N*-(2-picolyl)amino (IPA, hereafter) unit tethered to a tri(ethylene glycol) (TEG, hereafter) linker serves as the zinc chelator. The incorporation of the TEG moiety improves the solubility of JJ in aqueous solutions. Finally, cholesterol was introduced at the other end of the TEG linker in order to direct the probe to the outer surfaces of the plasma membranes of mammalian cells.[82] A control zinc probe without a TEG−cholesterol unit (JJC in Figure 1) was also synthesized to assess the localization ability of JJ.

JJ was synthesized with a ten-step synthesis; Scheme 1 illustrates the synthetic route. The preparation of JJ commenced with the tosylation of cholesterol. Nucleophilic substitution of the *p*-toluenesulfonate group with tri(ethylene glycol) afforded the TEG−cholesterol adduct (**2**) in a yield of 59%. The free hydroxyl group in the adduct was tosylated again, followed by substitution with imidazole-4-carbaldehyde in the presence of $K_2CO_3$ in $CH_3CN$. Reductive amination of the substitution product (**4**) and 2-picolylamine afforded the zinc receptor (**5**) in a moderate yield. The synthesis of the


https://dx.doi.org/10.1021/acs.inorgchem.0c01376
Inorg. Chem. XXXX, XXX, XXX−XXX

**Scheme 1. Synthesis of JJ**[a]

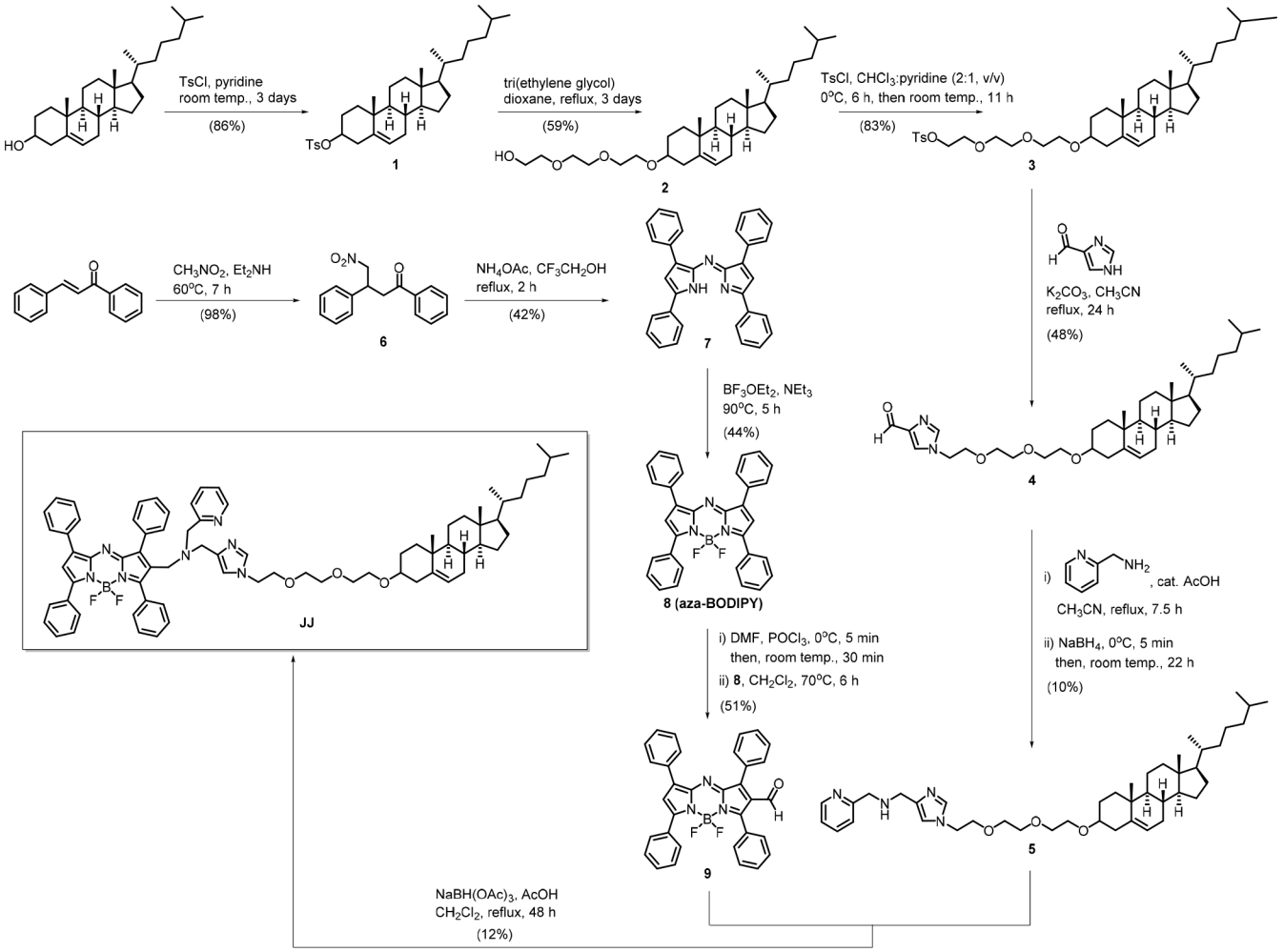


[a]The synthetic route for JJC is shown in the Supporting Information, Scheme S1.

deep-red fluorophore (aza-BODIPY) started with the Michael addition reaction of nitromethane into *trans*-chalcone. A three-component condensation of the Michael product (**6**) and $NH_4OAc$ in trifluoroethanol yielded the free-base aza-BODIPY (**7**). Borylation of **7** with $BF_3{\cdot}OEt_2$ furnished aza-BODIPY (**8**) in a yield of 51%. In order to introduce **5** into aza-BODIPY, **8** was formylated through the Villsmeyer−Haack reaction. Finally, JJ was obtained through reductive amination between **5** and the formylated aza-BODIPY (**9**). The details of the synthesis and structural characterization data are summarized in the Experimental Details section.

JJ exhibits high solubility in polar organic solvents, such as ethers, acetonitrile, and chlorinated solvents, but has moderate solubility in water. To prevent the aggregation of probes, an aqueous buffer (pH 7.4; 25 mM piperazine-*N*,*N*′-bis(2-ethanesulfonic acid) (PIPES), 100 mM KCl) containing 75 vol % DMSO was employed in the photophysical investigations. A solution of 100 mM KCl was employed to simulate the ionic strength of the biological milieu. Lower volume fractions of DMSO in buffers led to probe aggregation, resulting in inferior fluorescence zinc responses (Supporting Information, Figure S1). The partition coefficient (*clogP*), which was determined with the relationship $clogP = \log(C_0/C_w)$, where $C_0$ and $C_w$ are the concentrations of JJ in *n*-octane and the PIPES-buffered solution (pH 7.4, 100 mM KCl) respectively, is −0.47. This *clogP* value is much lower than that of aza-BODIPY (2.95), which indicates that JJ has better solubility in aqueous solutions.

**Zinc-Induced Fluorescence Turn-On.** Figure 2a shows the steady-state electronic absorption and emission spectra of 5 $\mu$M JJ in aqueous buffers (pH 7.4). JJ exhibits a strong absorption band with a peak wavelength ($\lambda_{abs}$) of 643 nm (molar absorbance ($\varepsilon$) = $3.68 \times 10^4$ $M^{-1}$ $cm^{-1}$). Upon photoexcitation at 622 nm, the zinc-free JJ solution exhibits deep-red fluorescence emission with a peak wavelength ($\lambda_{ems}$) of 663 nm and a photoluminescence quantum yield (PLQY) of 0.038. The electronic spectra of JJ are reminiscent of those of aza-BODIPY ($\lambda_{abs}$ = 655 nm ($\varepsilon = 3.02 \times 10^4$ $M^{-1}$ $cm^{-1}$); $\lambda_{ems}$ = 682 nm (PLQY = 0.30)), except for the low fluorescence intensity (Figure S2). The addition of 100 equiv of $ZnCl_2$ to the JJ solution results in a hypsochromic shift of the absorption peak wavelength to 637 nm ($\varepsilon = 3.62 \times 10^4$ $M^{-1}$ $cm^{-1}$). The zinc addition also elicits an approximately 5-fold enhancement in the fluorescence intensity. The zinc-rich JJ solution has a fluorescence peak wavelength of 662 nm with a PLQY of 0.21 (photoexcitation wavelength = 622 nm). The fluorescence dynamic range, which is defined as the fluorescence turn-on ratio × $\varepsilon_{622\ nm}$, is as large as 141000. The fluorescence sensing ability is not perturbed by the presence of the TEG−cholesterol unit because virtually identical zinc-induced


https://dx.doi.org/10.1021/acs.inorgchem.0c01376
Inorg. Chem. XXXX, XXX, XXX−XXX

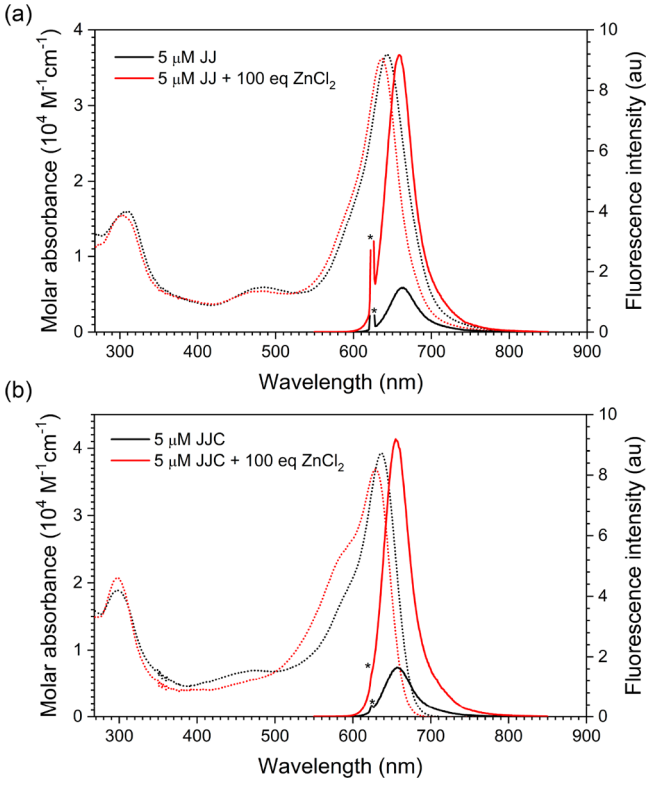


**Figure 2.** UV−vis absorption (dotted lines) and fluorescence (solid lines) spectra of (a) 5 $\mu$M JJ and (b) 5 $\mu$M JJC in the absence (black) and presence (red) of 100 equiv of $ZnCl_2$. Samples were dissolved in aqueous solutions containing 25 mM PIPES, 100 mM KCl, and 75 vol % DMSO buffered at pH 7.4. The peaks marked with an asterisk (*) correspond to the excitation beam ($\lambda_{ex}$ = 622 nm).

fluorescence turn-on (4.8) and dynamic range (153000) values are found for JJC (Figure 2b). The results indicate that the TEG−cholesterol unit does not perturb zinc coordination. Similarly, zinc responses with greater turn-on ratios were observed in $CH_3CN$ (Figure S3). Finally, the fluorescence zinc response of JJ is fully reversible, as is demonstrated by the recovery of the fluorescence spectrum to the zinc-free state upon the addition of *N*,*N*,*N*′,*N*′-tetrakis(2-picolyl)-ethylenediamine (TPEN), a strong zinc chelator (Figure 3).[83]

In order to identify the photophysical origin of the fluorescence response, we performed transient photoluminescence experiments in $CH_3CN$ (Figure S4). The fluorescence decay traces for 5 $\mu$M JJ were acquired with time-correlated single-photon-counting techniques after picosecond pulsed laser photoexcitation at 375 nm. A zinc-free solution of JJ produces a biphasic exponential decay with a weighted average lifetime ($\tau_{obs}$) of 0.23 ns. The $\tau_{obs}$ value increases to 1.3 ns upon the addition of 100 equiv of zinc ions. The zinc-induced increase in $\tau_{obs}$ corresponds to a one order of magnitude decrease in the nonradiative decay rate ($k_{nr}$) from $42 \times 10^8$ $s^{-1}$ (zinc-free state) to $6.1 \times 10^8$ $s^{-1}$ (zinc-bound state), while the radiative decay rate ($k_r$) remains relatively unaltered (zinc-free state, $1.7 \times 10^8$ $s^{-1}$; zinc-bound state, $1.6 \times 10^8$ $s^{-1}$). Qualitatively identical changes were also found for JJC (zinc-free state, $k_r = 2.9 \times 10^8$ $s^{-1}$, $k_{nr} = 53 \times 10^8$ $s^{-1}$; zinc-bound state, $k_r = 3.0 \times 10^8$ $s^{-1}$, $k_{nr} = 8.4 \times 10^8$ $s^{-1}$). This nonradiative control indicates the presence of a fluorescence-quenching process that is abolished by zinc binding.

Figure 4 compares the cyclic and differential pulse voltammograms of aza-BODIPY, JJC, and JJ. Aza-BODIPY exhibits reversible one-electron reduction at a potential ($E_{red}$) of −0.80 V vs $Fc^+/Fc$. The oxidation process is irreversible, and the differential pulse voltammogram shows that the oxidation potential ($E_{ox}$) is at 0.81 V vs $Fc^+/Fc$. The corresponding electrochemical bandgap energy (1.61 eV) is comparable to the optical bandgap energy ($\Delta E_g$, 1.82 eV) determined from the fluorescence peak wavelength ($\lambda_{ems}$ = 682 nm). For JJC, the first $E_{ox}$ is at 0.04 V vs $Fc^+/Fc$, i.e., it is cathodically shifted from that (0.81 V vs $Fc^+/Fc$) of aza-BODIPY. It is reasonable to assign this oxidation to originate in the tertiary amino group in the zinc receptor. In contrast, the first reduction potential of JJC is identical to that of aza-BODIPY. This electrochemical alignment permits photo-induced one-electron transfer from the zinc receptor to the excited-state aza-BODIPY. The excited-state reduction poten-

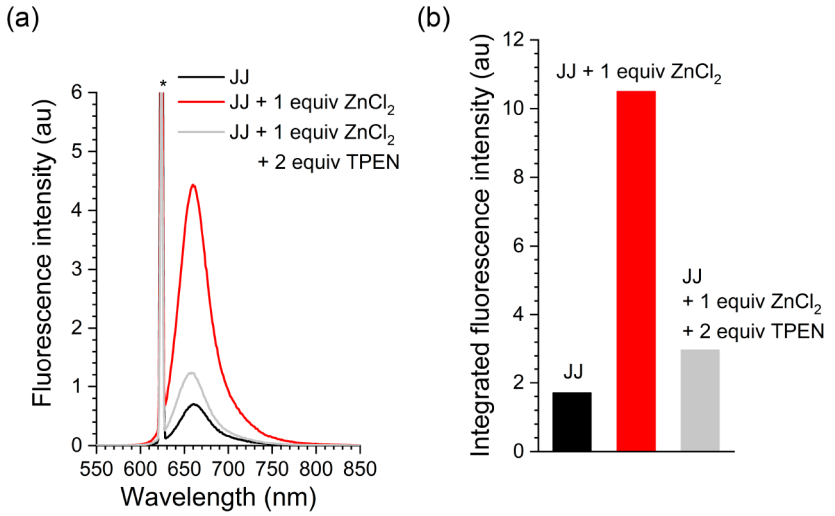


**Figure 3.** Reversible fluorescence zinc sensing of JJ. (a) Fluorescence spectra and (b) the corresponding integrated fluorescence intensities of 5 $\mu$M JJ in the absence (black) and presence (red) of 1 equiv of $ZnCl_2$ and after subsequent addition of 2 equiv of TPEN (gray). Samples were dissolved in aqueous solutions containing 25 mM PIPES, 100 mM KCl, and 75 vol % DMSO buffered at pH 7.4. The peaks marked with an asterisk (*) correspond to the excitation beam ($\lambda_{ex}$ = 622 nm).


https://dx.doi.org/10.1021/acs.inorgchem.0c01376
Inorg. Chem. XXXX, XXX, XXX−XXX

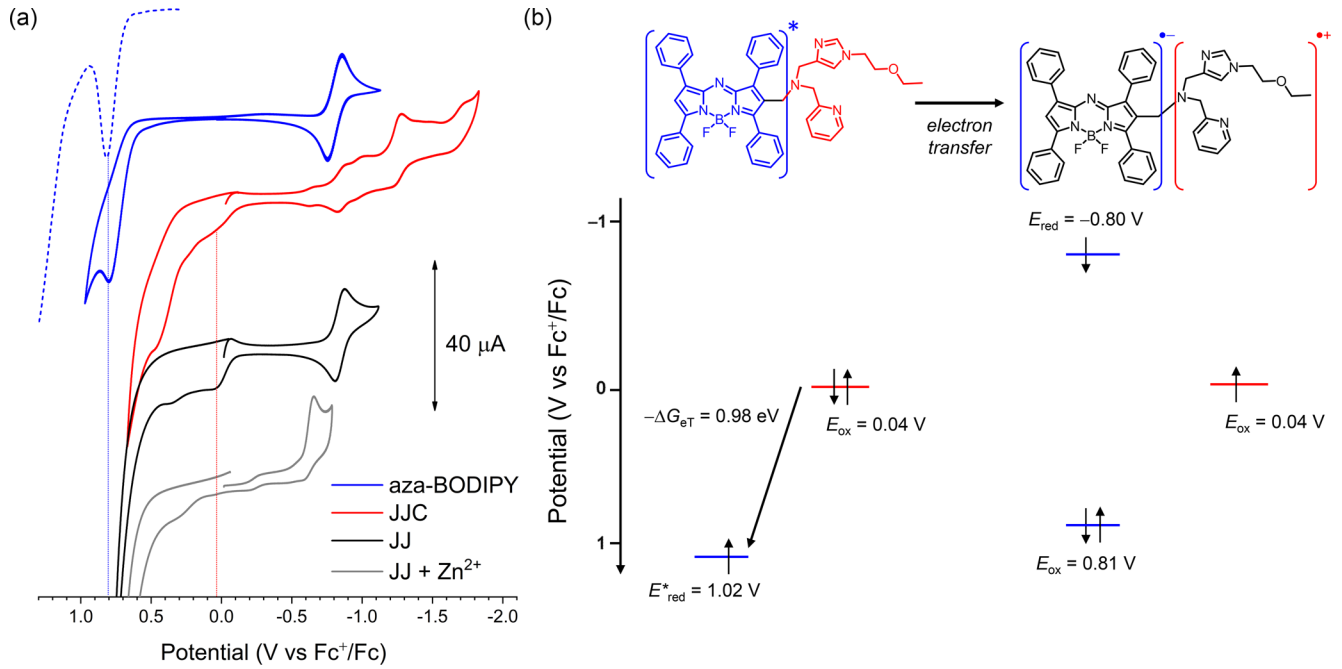


**Figure 4.** Driving force for intramolecular photoinduced one-electron transfer. (a) Cyclic (CV, solid curves) and differential pulse (DPV, dashed curves) voltammograms of 2.0 mM aza-BODIPY (blue), 2.0 mM JJC (red), and 2.0 mM JJ in the absence (black) and presence (gray) of 10 equiv of $Zn(ClO_4)_2$ obtained in Ar-saturated THF/DMSO (4:1, v/v) containing 0.10 M $TBAPF_6$ supporting electrolyte. A Pt disk and a Pt wire were used as the working and counter electrodes, respectively, and an $Ag/AgNO_3$ (10 mM) pseudo-reference electrode was used (scan rate = 0.10 V $s^{-1}$ (CV) and 4 mV $s^{-1}$ (DPV)). The vertical blue and red dotted lines indicate the one-electron oxidation of aza-BODIPY and the tertiary amino units in JJ and JJC, respectively. (b) Electrochemical potentials of the photoexcited JJC (left) and the charge-separated state of JJC (right). The black arrow indicates photoinduced one-electron transfer with a driving force of 0.98 eV.

**Table 1. Photophysical Parameters of JJ, JJC, and Aza-BODIPY**

| | $\lambda_{abs}$ (nm) /$\varepsilon$ ($10^4$ $M^{-1}$ $cm^{-1}$)[a] | | $\lambda_{ems}$ (nm) /PLQY[a,b] | | | | | |
|---|---|---|---|---|---|---|---|---|
| | no $ZnCl_2$ | 100 equiv of $ZnCl_2$ | no $ZnCl_2$ | 100 equiv of $ZnCl_2$ | turn-on ratio/DR[a,c] | $\tau_{obs}$ (ns) (100 equiv of $Zn^{2+}$ /no $Zn^{2+}$)[d,e] | $k_r$ ($10^8$ $s^{-1}$) (100 equiv of $Zn^{2+}$ /no $Zn^{2+}$)[d,f] | $k_{nr}$ ($10^8$ $s^{-1}$) (100 equiv of $Zn^{2+}$ /no $Zn^{2+}$)[d,g] |
| JJ | 643/3.68 | 637/3.62 | 663/0.038 | 662/0.21 | 5.4/141000 | 1.3/0.23 | 1.6/1.7 | 6.1/42 |
| JJC | 636/3.93 | 629/3.69 | 657/0.053 | 655/0.26 | 4.8/153000 | 0.88/0.18 | 3.0/2.9 | 8.4/53 |
| aza-BODIPY | 655/3.02 | –[h] | 682/0.30 | –[h] | –[h] | –[h] | –[h] | –[h] |

[a] 5 $\mu$M in aqueous solutions containing 25 mM PIPES, 100 mM KCl, and 75 vol % DMSO buffered at pH 7.4. Data obtained with differed volume fractions of DMSO are collected in Table S1. [b] $\lambda_{ex}$ = 622 nm. Photoluminescence quantum yield (PLQY) determined relative to the 9,10-diphenylanthracene standard (toluene, PLQY = 1.0).[85] [c] Dynamic range (DR) corresponds to DR = turn-on ratio × $\varepsilon_{622\ nm}$ (zinc-free). [d] 5 $\mu$M in Ar-saturated $CH_3CN$. [e] Weighted average fluorescence lifetime, $\tau_{obs} = (\Sigma a_i \times \tau_i^2)/(\Sigma a_i \times \tau_i)$ ($i$ = 1–2), where $a_i$ and $\tau_i$ are the pre-exponential factor and the time constant, respectively. [f] Radiative decay rate, $k_r = PLQY_{CH3CN}/\tau_{obs}$. [g] Nonradiative decay rate, $k_{nr} = (1 - PLQY_{CH3CN})/\tau_{obs}$. The $PLQY_{CH3CN}$ values in $k_r$ and $k_{nr}$ were determined in Ar-saturated $CH_3CN$: JJ, 0.0055 (no $Zn^{2+}$) and 0.35 (100 equiv of $Zn^{2+}$); JJC, 0.0049 (no $Zn^{2+}$) and 0.23 (100 equiv of $Zn^{2+}$). [h] Not determined.

tial ($E^*_{red}$) of aza-BODIPY (or JJC) was calculated to be 1.02 V vs $Fc^+/Fc$ by using the relationship $E^*_{red} = E_{red} + \Delta E_g$. This $E^*_{red}$ value is more positive than the $E_{ox}$ value (0.04 V vs $Fc^+$/Fc) of the zinc receptor. The driving force for one-electron transfer ($-\Delta G_{eT}$) is as large as 0.98 eV according to the Rehm–Weller equation $-\Delta G_{eT} = e \times [E_{ox}$ (zinc receptor) $- E^*_{red}$ (aza-BODIPY)], where $e$ is the elementary charge.[84] JJ is predicted to enable the same photoinduced intramolecular electron transfer because it exhibits a bandgap energy and electrochemical potentials identical to those of JJ (Figure 4a). The addition of zinc ions into the JJ solution results in the disappearance of the first oxidation ($E_{ox}$ = 0.04 V vs $Fc^+/Fc$), which suggests thermodynamic disallowance of the electron transfer. Taking these results together, we conclude that the zinc-induced fluorescence turn-on response is due to the abrogation of intramolecular photoinduced electron transfer. It has been challenging to modulate photoinduced electron transfer involving deep-red emitters.[86−88] Therefore, our demonstration is a significant one. The photophysical data for JJ, JJC, and aza-BODIPY are summarized in Table 1.

**Fluorescence Zinc Detection.** A fluorescence Job plot indicates that the binding of JJ with zinc ions is 1:1 (Figure S5). In order to assess the zinc detection ability, zinc titration experiments were performed. Figure 5 shows the fluorescence spectra of 5 $\mu$M JJ recorded in various zinc-buffered solutions at pH 7.4 (free zinc concentration ($[Zn]_{free}$) = 0.15 pM to 120 nM; 100 mM *N*-(2-hydroxyethyl)piperazine-*N*′-(2-ethanesulfonic acid) (HEPES), 100 mM $NaNO_3$, 10 mM *N*-(2-hydroxyethyl)ethylenediamine-*N*,*N*′,*N*′-triacetic acid (HEDTA), and $ZnSO_4$). The corresponding fluorescence


https://dx.doi.org/10.1021/acs.inorgchem.0c01376
Inorg. Chem. XXXX, XXX, XXX–XXX

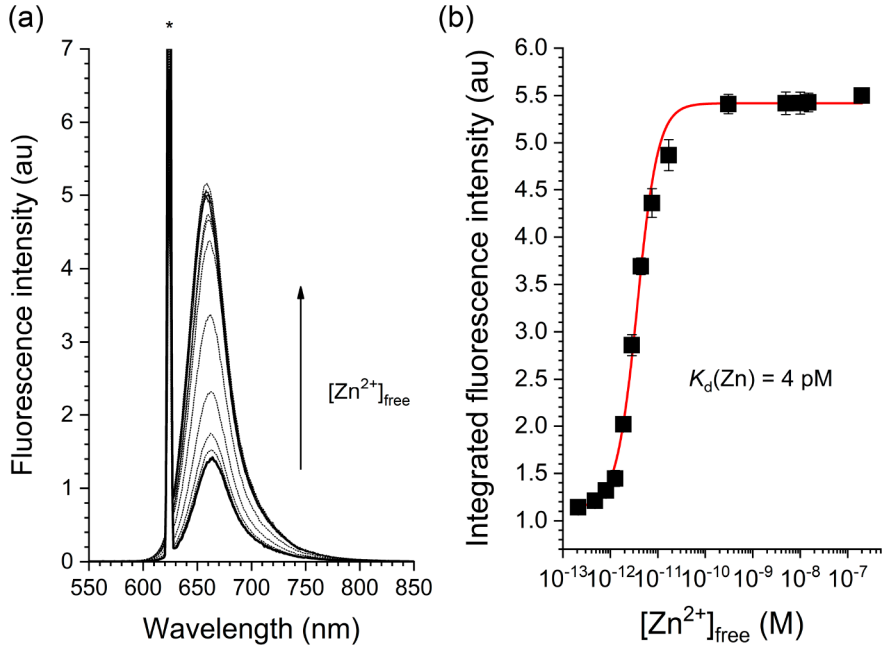


**Figure 5.** Determination of the zinc dissociation constant ($K_d$ (Zn)) of JJ. (a) Fluorescence spectra of 5.0 $\mu$M JJ obtained in 15 zinc-buffered aqueous solutions (pH 7.4; 100 mM HEPES, 100 mM $NaNO_3$, 10 mM HEDTA, and $ZnSO_4$). (b) Corresponding fluorescence zinc titration isotherm (black squares) and a nonlinear least-squares fit to a 1:1 binding model (red curve). The peak marked with an asterisk (*) in (a) corresponds to the excitation beam ($\lambda_{ex}$ = 622 nm). The error bars were obtained from three experiments.

titration isotherm has a typical sigmoidal form. A nonlinear least-squares fit of the isotherm to a 1:1 binding model indicated that the zinc dissociation constant ($K_d$ (Zn)) is 4 pM. A similar $K_d$ (Zn) was found for JJC (3 pM) (Figure S6). These tight-binding behaviors are comparable to those of a previous BODIPY-based probe bearing a structurally similar di(2-picolyl)amine zinc receptor.[89] Note that the zinc-binding affinity depends sensitively on the volume fraction of DMSO. A nonsigmoidal behavior is found for the fluorescence zinc titration isotherm at an increased (80 vol %) DMSO fraction (Figure S7).

The fluorescence zinc signaling of JJ is hardly perturbed by pH changes. The fluorescence intensity is weak at basic pH values and starts to increase for pH < 7. As shown in Figure 6, pH titration experiments show that p$K_a$ is as low as 5.9. The p$K_a$ of JJC is 6.1, which is close to that of JJ (Figure S8). This similarity suggests that the fluorescence increase results from the protonation of the zinc receptor. However, it is inferred from the p$K_a$ value that the protonation-induced fluorescence artifact is minimal at physiologically relevant pH values (~7.4). Note that the fluorescence turn-on response is preserved at low pH values (Figure 6c). This pH tolerance is ascribed to tight zinc binding; the zinc association is 300000-fold stronger than the proton association according to the ratio $K_a/K_d$(Zn).

The fluorescence signaling of JJ is selective to zinc over biological metal ions. The presence of 1.0 mM NaCl, 100 $\mu$M $MgCl_2$, and 1.0 mM $CaCl_2$ does not interfere with the fluorescence zinc response of 5 $\mu$M JJ (Figure 7). The presence of 10 $\mu$M biologically important transition-metal ions, including Cr, Mn, Fe, Co, and Ni, does not perturb zinc binding. The Cu ion competes with zinc for coordination with JJ, but zinc coordination appears stronger than copper binding because a prompt turn-on response is elicited upon the addition of zinc to a mixture of JJ and $CuCl_2$. Finally, the fluorescence zinc response is not affected by the presence of Cd and Hg ions, which are strong competitors of zinc toward coordination. Virtually identical zinc selectivity is observed for JJC (Figure S9). From the results of the cuvette experiments, we conclude that JJ exhibits turn-on responses exclusively to zinc ions.

**Fluorescence Visualization of Cellular Zinc.** To assess the usefulness of our probe in bioimaging, live HeLa cells were treated with JJ. NucBlue Live/NucGreen Dead assays indicate that the cytotoxicity of JJ is low; NucBlue Live and NucGreen Dead selectively stain live and dead cells, respectively. Figure 8a demonstrates that the majority of HeLa cells are stained blue (i.e., live) when they are incubated with 0.4 and 0.8 $\mu$M JJ (10 min). Increases in the JJ concentration to 2 and 20 $\mu$M (10 min) lead to cell death, as can be seen in the emergence of cells stained green. Similar results were obtained in MTT cell viability assays (Figure 8c). The cell survival curve starts to decay for JJ concentrations >1 $\mu$M (2 h incubation at 37 °C). These viability results and the red fluorescence emission of JJ (Figure 8a) ensures that there is perceptible zinc imaging after incubation at submicromolar concentrations.

Figure 9 compares the fluorescence micrographs of HeLa cells coincubated with organelle-specific fluorescence stains, including nuclear stain, endoplasmic reticulum stain, lysosomal stain, mitochondrial stain, and membrane stain. The overlay images reveal that the fluorescent puncta of JJ overlap with those of lysosomes and endoplasmic reticula. Pearson's colocalization coefficients are 0.82 and 0.61 for the former and latter, respectively. In contrast, the Pearson's colocalization coefficient for the membrane stain is 0.12. JJC, the control probe devoid of the TEG−cholesterol unit, is also found to localize within the endoplasmic reticula and lysosomes (Figure S10). The results suggest that the aza-BODIPY−zinc receptor unit (i.e., JJC moiety) is responsible for the localization within the lysosomes and endoplasmic reticula.


https://dx.doi.org/10.1021/acs.inorgchem.0c01376
Inorg. Chem. XXXX, XXX, XXX−XXX

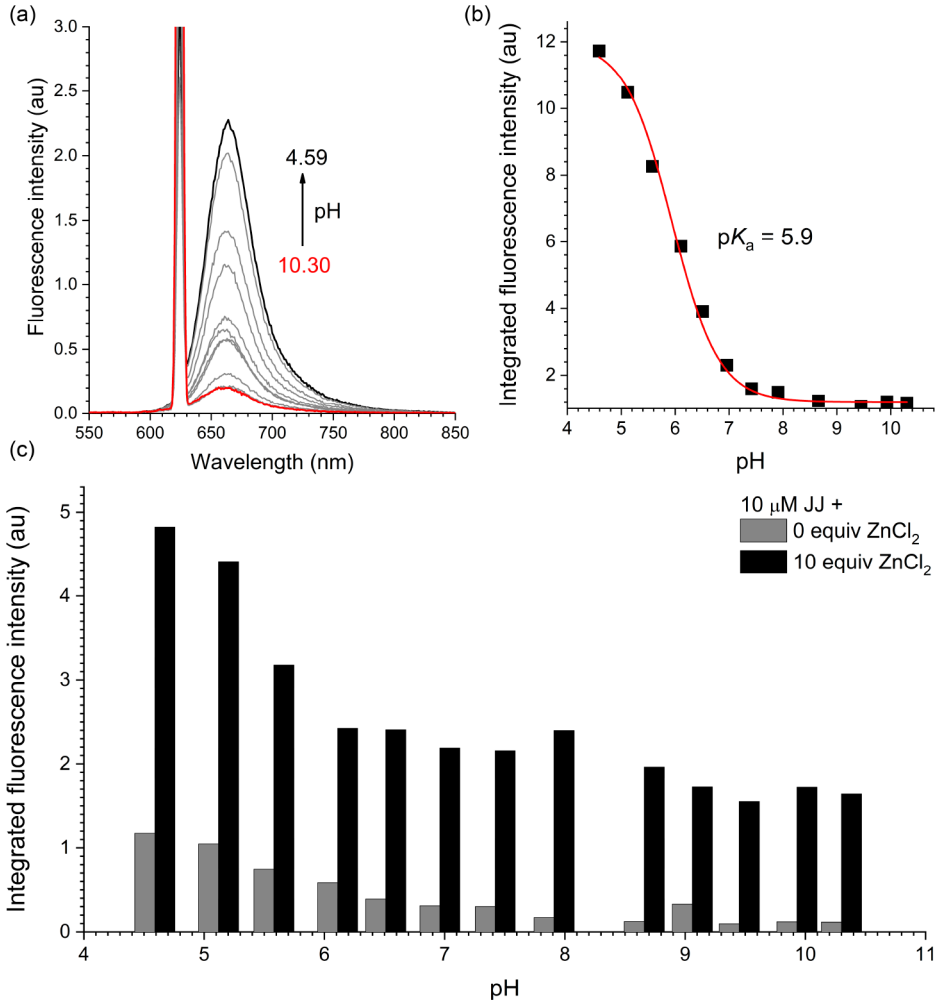


**Figure 6.** pH tolerance of the fluorescence zinc responses of JJ. (a) Fluorescence spectra of 10 $\mu$M JJ in an aqueous solution (75 vol % DMSO) containing 100 mM KCl for various pH values (10.30 to 4.59). (b) The corresponding fluorescence pH titration isotherm (black squares) and its nonlinear least-squares fit to the equation FI = $(AK_a + B[H^+])/([H^+] + K_a)$ (red curve), where FI is the integrated fluorescence intensity and $A$ and $B$ are fitting constants. (c) Integrated fluorescence intensities of 10 $\mu$M JJ in the absence (gray bars) and presence (black bars) of 10 equiv of $ZnCl_2$ at various pH values.

This poor localization at the plasma membrane indicates that the internalization of JJ is rapid after extracellular membrane anchoring. Actually, live imaging experiments reveal prompt anchoring of JJ at the plasma membrane of HeLa cells, followed by subsequent uptake into cytoplasm (Figure S11 and Movie S1). To determine the internalization mechanism, HeLa cells were treated with 0.4 $\mu$M JJ under various conditions. Figure 10 shows that the intracellular uptake of JJ is retarded upon incubation at 4 °C or upon pretreatment with metabolic inhibitors (50 mM 2-deoxy-D-glucose/5 $\mu$M oligomycin) or endocytic inhibitors (5 $\mu$M chloroquine or 50 mM $NH_4Cl$).[90,91] This retardation suggests that the cellular entry of JJ occurs via various mechanisms, including passive diffusion, active transport, and endocytosis. The rapid uptake of JJ could be a corollary of the presence of a multitude of intracellular uptake pathways.

Finally, the fluorescence zinc detection of JJ was evaluated (Figure 11a). HeLa cells were incubated with 0.2 $\mu$M JJ for 20 min. JJ was internalized into the cells and found to exhibit weak fluorescence intensities. An addition of 20 $\mu$M $ZnCl_2$ into the extracellular medium elicits an approximately 2-fold fluorescence enhancement. This zinc response is unexpected because it is not anticipated that $ZnCl_2$ will penetrate the cell membrane without the help of a pyrithione (PT) ionophore. Subsequent treatments with 200 $\mu$M ethylenediaminetetraacetic acid (EDTA), a cell-impermeable metal chelator, restored the fluorescence intensity to the original state. Identical behaviors were also found for JJ-treated DLD-1 cells (Figure S12). The observed fluorescence switching with $ZnCl_2$ and EDTA indicates that JJ permeabilized the cell membrane. In sharp contrast, JJC devoid of the TEG–cholesterol moiety does not evoke such permeabilization (Figure 11b). Fluorescence turn-on responses are produced only when $ZnCl_2$ is present together with the PT ionophore. These results suggest that the membrane-targeting TEG–cholesterol unit has an antagonistic effect. This observation is consistent with the results of the groups of Städler and Wüstner, where cholesterol has large effects on membrane permeability.[82,92] Anchored cholesterol can increase the free volume of a lipid bilayer and, thereby, facilitates the diffusion and transport of exogens.[93] Our research shows that the judicious use of cholesterol is essential for the immobilization of probes.


https://dx.doi.org/10.1021/acs.inorgchem.0c01376
Inorg. Chem. XXXX, XXX, XXX−XXX

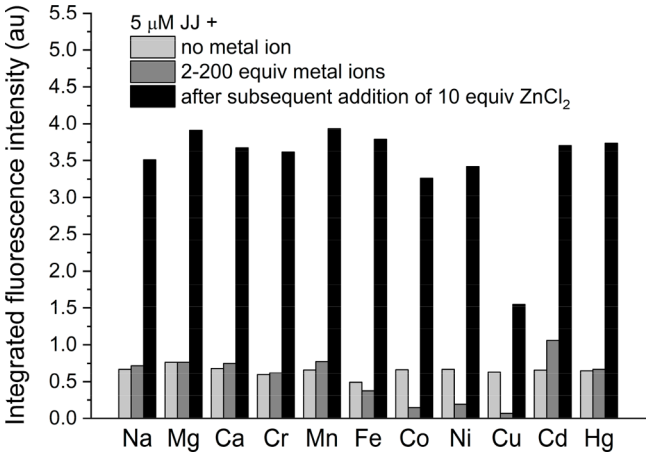


**Figure 7.** Fluorescence selectivity of JJ for zinc over biological metal ions. Integrated fluorescence intensities of 5 $\mu$M JJ in the absence (light gray bars) and presence (dark gray bars) of competing metal ions and after the subsequent addition of 10 equiv of $ZnCl_2$ (black bars) (25 mM PIPES, 100 mM KCl, and 75 vol % DMSO buffered at pH 7.4): 1.0 mM NaCl, 100 $\mu$M $MgCl_2$, 1.0 mM $CaCl_2$, and 10 $\mu$M other metal chlorides.

## SUMMARY AND CONCLUSIONS

Fluorescence zinc probes targeting specific organelles are valuable because they enable the monitoring of intra- and intercellular zinc trafficking. We have designed a deep-red fluorescent zinc probe (JJ) with a focus on bioimaging utility. Aza-BODIPY was modified with a *N*-(4-imidazolyl)-*N*-(2-picolyl)amino zinc receptor, which was tethered to a membrane-targeting cholesterol unit through a tri(ethylene glycol) linker. JJ exhibits a reversible, approximately 5-fold turn-on response to zinc ions in the deep-red emission region ($\lambda_{ems}$ = 662 nm) in aqueous solutions buffered to pH 7.4. We demonstrated that the fluorescence zinc signaling of our probe is not affected by changes in pH and the presence of biological metal ions. This high zinc selectivity is due to tight zinc binding with a dissociation constant of 4 pM. Our spectroscopic and electrochemical results show that electron transfer occurs from the zinc receptor to photoexcited aza-BODIPY to form a nonemissive, intramolecularly charge-separated species with a driving force of 0.98 eV. The zinc binding of JJ abrogated the nonradiative photoinduced electron transfer to restore the inherent emission of aza-BODIPY. JJ is nontoxic to HeLa cells, which implies that it can be used for bioimaging in the deep-red-fluorescence region. Unexpectedly, JJ was found to leak across the outer surface of the plasma membrane and to internalize rapidly in the lysosomes and endoplasmic reticula of HeLa cells. Our cellular experiments have shown that the intracellular entry of JJ involve a multitude of uptake mechanisms. This probe internalization permeabilizes the plasma membrane, which permits the influx of exogenous zinc ions into the intracellular

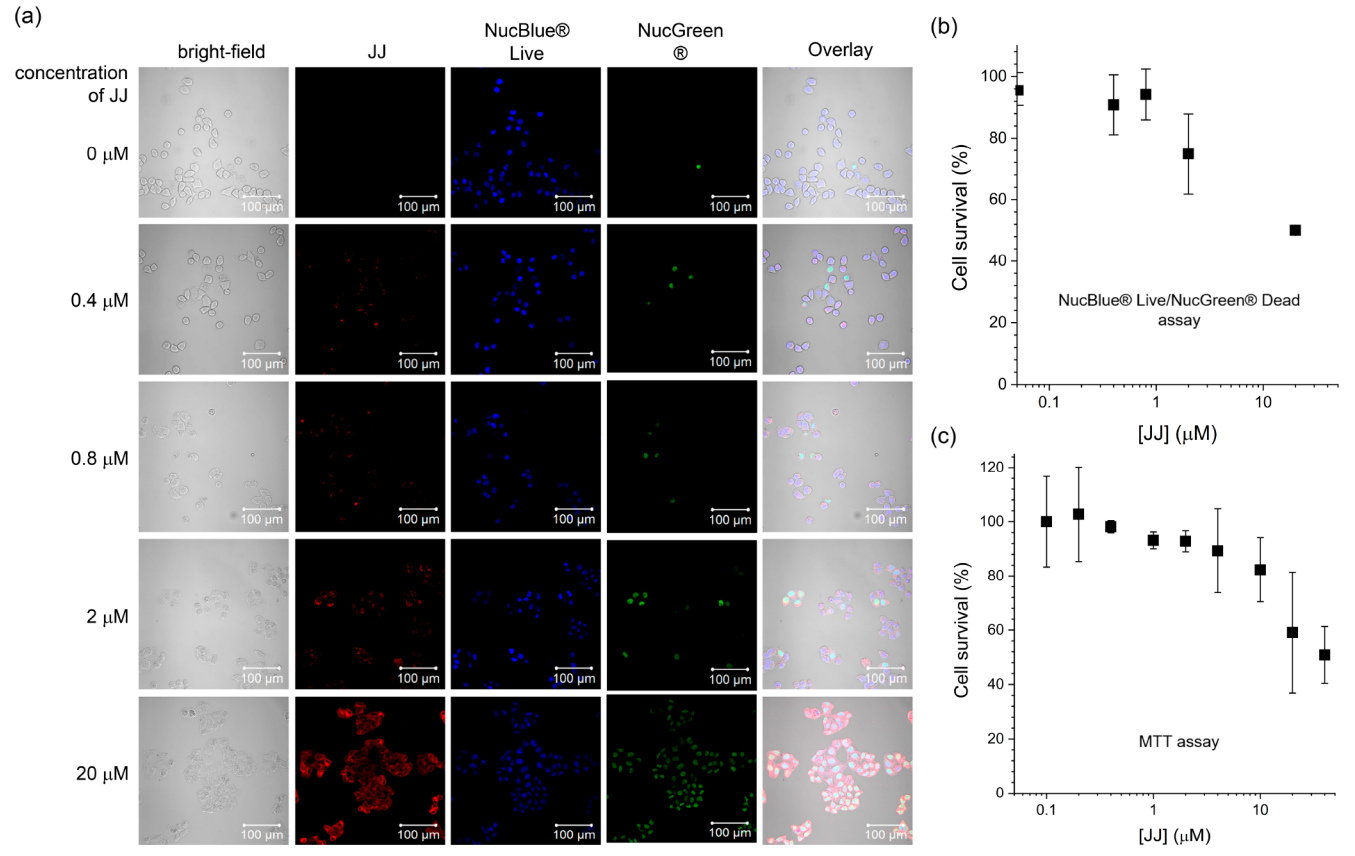


**Figure 8.** Cytotoxicity of JJ. (a) Micrographs showing the NucBlue Live/NucGreen Dead assay of HeLa cells treated with 0, 0.4, 0.8, 2, and 20 $\mu$M JJ for 10 min. From the left, bright-field images, micrographs showing JJ fluorescence ($\lambda_{ex}$ = 633 nm, $\lambda_{em}$ = 640–677 nm), NucBlue Live fluorescence ($\lambda_{ex}$ = 488 nm, $\lambda_{em}$ = 415–460 nm), and NucGreen Dead fluorescence ($\lambda_{ex}$ = 561 nm, $\lambda_{em}$ = 499–552 nm), and overlay images are shown. Scale bar = 100 $\mu$m. (b) Corresponding percent cell survival results. % cell survival = 100 × (number of live cells)/(number of total cells). (c) MTT cell proliferation assay results. HeLa cells were treated with 0.1–40 $\mu$M JJ at 37 °C for 2 h.


https://dx.doi.org/10.1021/acs.inorgchem.0c01376
Inorg. Chem. XXXX, XXX, XXX–XXX

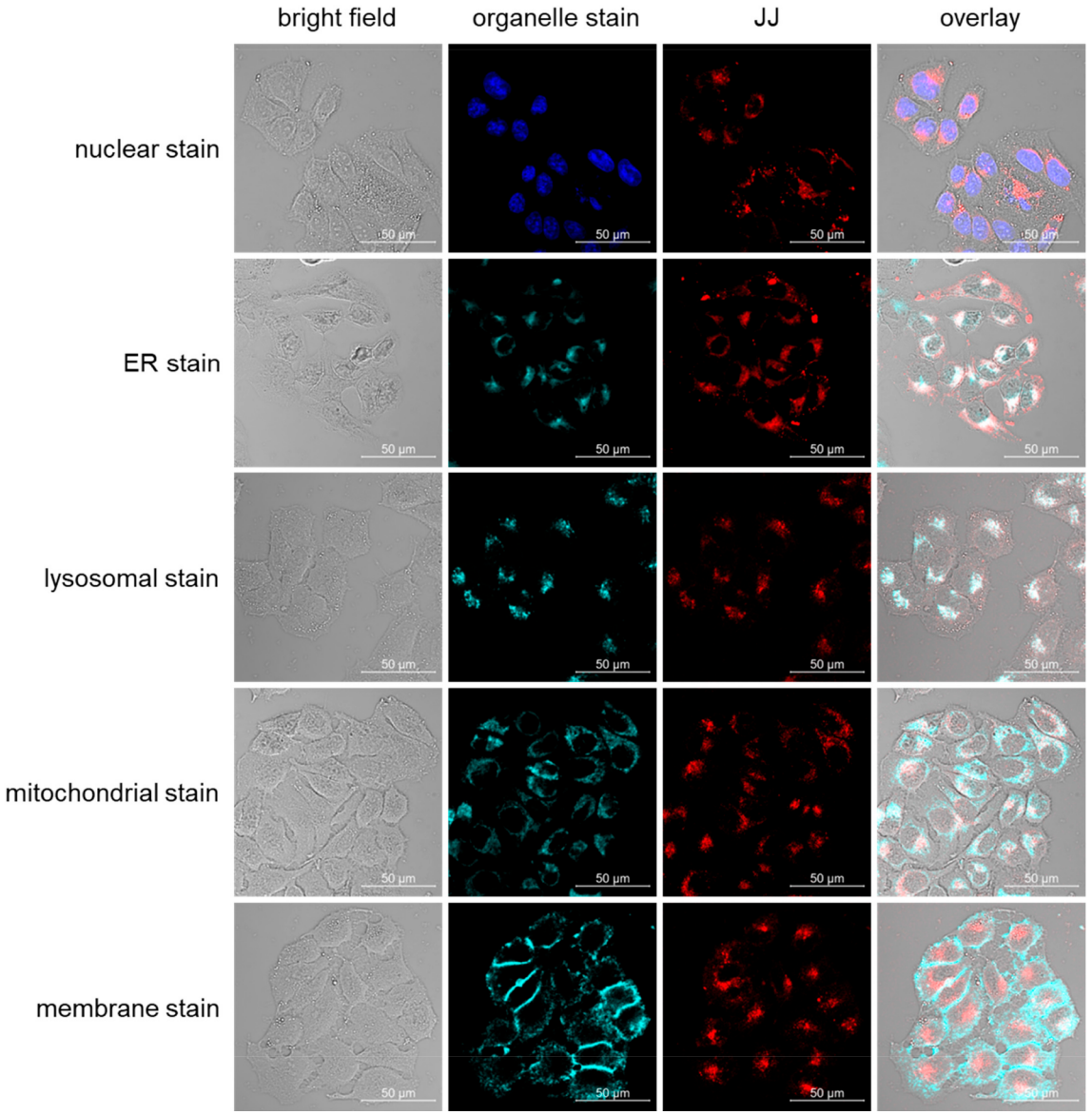


**Figure 9.** Intracellular localization of JJ in HeLa cells. First column panels, bright images; second column panels, fluorescence images of organelle-specific stains; third column panels, fluorescence images of JJ (0.2 $\mu$M, 10 min, $\lambda_{ex}$ = 633 nm/$\lambda_{em}$ = 646−684 nm); fourth column panels, overlay images. From the top: nuclear stain, DAPI (300 nM, 5 min, $\lambda_{ex}$ = 488 nm/$\lambda_{em}$ = 417−456 nm); endoplasmic reticulum (ER) stain, ER−Tracker Green (1 $\mu$M, 20 min, $\lambda_{ex}$ = 488 nm/$\lambda_{em}$ = 498−553 nm); lysosomal stain, LysoTracker Green (75 nM, 30 min, $\lambda_{ex}$ = 488 nm/$\lambda_{em}$ = 498−553 nm); mitochondrial stain, MitoTracker Green (200 nM, 15 min, $\lambda_{ex}$ = 488 nm/$\lambda_{em}$ = 498−553 nm); membrane stain, CellMask Green Plasma Membrane (×1000, 5 min, $\lambda_{ex}$ = 488 nm/$\lambda_{em}$ = 498−553 nm). Pearson's colocalization coefficients: nuclei, 0.17; endoplasmic reticula, 0.61; lysosome, 0.82; mitochondria, 0.26; plasma membrane, 0.12. Scale bar = 50 $\mu$m.

compartments. A control probe that does not contain a cholesterol unit was found not to elicit such permeabilization. These results demonstrate that careful structural control is required to obtain fluorescence signaling without altering cellular function.

## EXPERIMENTAL SECTION

**Materials and Structural Identification.** Commercially available chemicals were used as received unless otherwise stated. $^{1}$H and $^{13}$C{$^{1}$H} NMR spectra were collected with Bruker Ultrashield 500 and 300 plus NMR spectrometers. Chemical shifts were referenced to $(CH_3)_4Si$. High-resolution mass spectra (positive mode, FAB, *m*−NBA) were obtained by employing a JEOL, JMS-600W mass spectrometer.

**Synthesis of 1.** Cholesterol (100 g, 259 mmol) was dissolved in pyridine (350 mL) in a one-necked round-bottom flask equipped with a magnetic stir bar. After the slow addition of *p*-toluenesulfonyl chloride (54.2 g, 284 mmol), the reaction mixture was stirred for 3 days at room temperature. Water (400 mL) was poured onto the solution, and the crude product was extracted with diethyl ether (400 mL × three times). The collected organic layer was dried over anhydrous $MgSO_4$. Concentration under reduced pressure afforded a white powder in an 86% yield. $R_f$ = 0.7 ($CH_2Cl_2$). $^{1}$H NMR (300 MHz, $CDCl_3$) $\delta$ (ppm): 0.65 (s, 3H), 0.86 (dd, $J$ = 6.6, 1.5 Hz, 6H), 0.90 (d, $J$ = 6.6 Hz, 3H), 0.96 (s, 3H), 2.45 (s, 3H), 4.32 (m, 1H), 5.30 (d, $J$ = 5.4 Hz, 1H), 7.33 (d, $J$ = 8.1 Hz, 2H), 7.80 (d, $J$ = 8.1 Hz, 2H). $^{13}$C{$^{1}$H} NMR (126 MHz, $CDCl_3$) $\delta$ (ppm): 11.8, 18.7, 19.2, 21.0, 21.7, 22.6, 22.8, 23.8, 24.3, 28.0, 28.2, 28.6, 31.7, 31.9, 35.8, 36.2, 36.4, 36.9, 38.9, 39.5, 39.7, 42.3, 49.9, 56.1, 56.7, 82.4, 123.5, 127.7, 129.7, 134.7, 138.9, 144.4.

**Synthesis of 2.** Compound **1** (40.0 g, 74.0 mmol) and tri(ethylene glycol) (20.0 mL, 151 mmol) were combined in a 1 L one-necked round-bottom flask. The reaction mixture was dissolved


https://dx.doi.org/10.1021/acs.inorgchem.0c01376
Inorg. Chem. XXXX, XXX, XXX−XXX

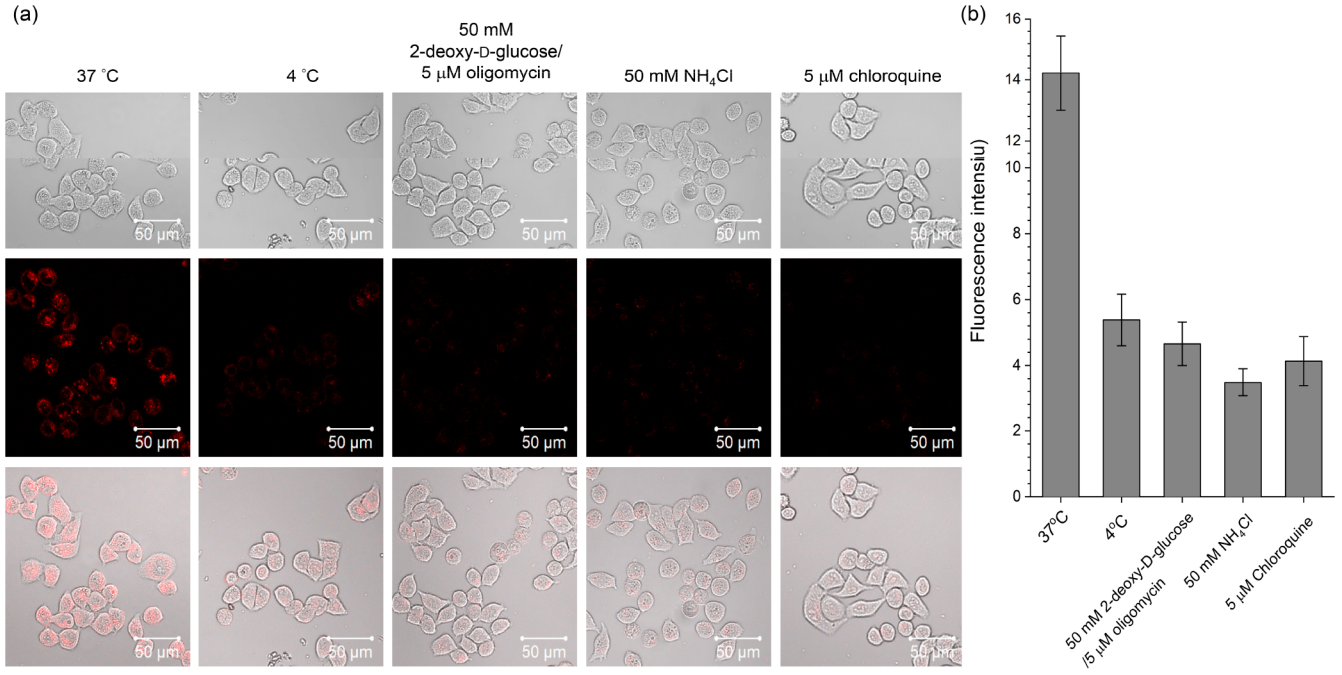


**Figure 10.** Intracellular uptake of JJ. (a) Micrographs showing HeLa cells treated with 0.4 $\mu$M JJ (10 min) under various conditions. Top panels, bright-field images; middle panels, fluorescence images ($\lambda_{ex}$ = 633 nm, $\lambda_{em}$ = 640−677 nm); bottom panels, overlay images. Scale bar = 50 $\mu$m. (b) Corresponding fluorescence intensities of the HeLa cells. Error bars were determined from five dishes treated independently.

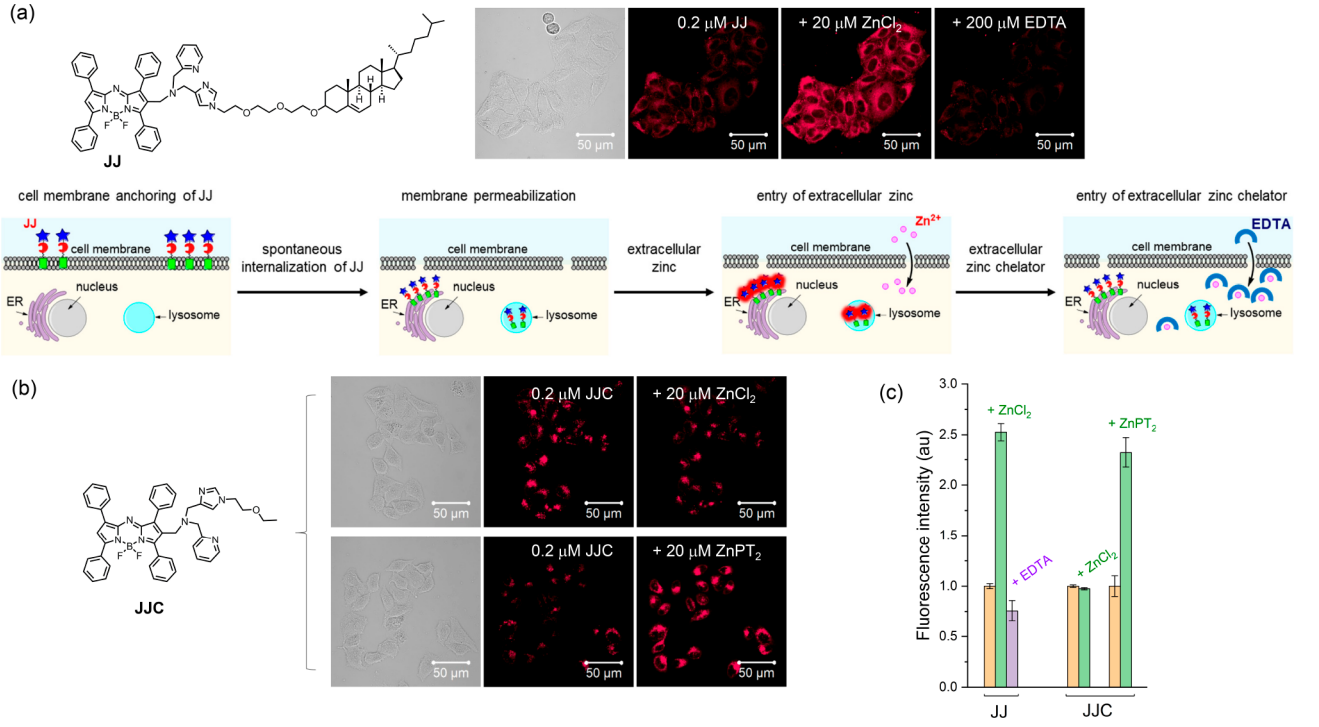


**Figure 11.** Visualization of intracellular zinc ions. (a) Top panels, bright-field (1st panel) and fluorescence micrographs (2nd to 4th panels) of HeLa cells treated with 0.2 $\mu$M JJ (20 min), after subsequent incubation with 20 $\mu$M $ZnCl_2$ (5 min), and finally, after the addition of 200 $\mu$M EDTA. Bottom panels, schematic representation of the JJ-induced permeabilization of the cell membranes. (b) Top panels, bright-field (1st panel) and fluorescence micrographs (2nd and 3rd panels) of HeLa cells treated with 0.2 $\mu$M JJC (20 min) and after subsequent incubation with 20 $\mu$M $ZnCl_2$ (15 min); bottom panels, bright-field (1st panel) and fluorescence micrographs (2nd and 3rd panels) of HeLa cells treated with 0.2 $\mu$M JJC (20 min) and after subsequent incubation with 20 $\mu$M $ZnPT_2$ (15 min). (c) The corresponding fluorescence intensities of the fluorescence micrographs. Error bars were determined from five dishes treated independently.

in dioxane (400 mL) and refluxed for 3 days. After it cooled to room temperature, the reaction mixture was poured onto water (400 mL). The crude product was recovered by extracting it with EtOAc (400 mL × three times). The organic layer was washed with a 5% aqueous solution of $KHCO_3$ and water, dried over anhydrous $MgSO_4$, filtered, and concentrated under reduced pressure. Purification via silica gel


https://dx.doi.org/10.1021/acs.inorgchem.0c01376
Inorg. Chem. XXXX, XXX, XXX−XXX

column chromatography was performed with employing diethyl ether/EtOAc = 8:2 (v/v) as an eluent to give a white solid in a 59% yield. $R_f$ = 0.3 (diethyl ether/EtOAc = 8:2, v/v). $^1$H NMR (300 MHz, $CDCl_3$) $\delta$ (ppm): 0.67 (s, 3H), 0.86 (dd, $J$ = 6.6, 1.5 Hz, 6H), 0.91 (d, $J$ = 6.6 Hz, 3H), 1.00 (s, 3H), 3.19 (m, 1H), 3.68 (m, 12H), 5.34 (d, $J$ = 5.4 Hz, 1H). $^{13}$C{$^1$H} NMR (126 MHz, $CDCl_3$) $\delta$ (ppm): 11.9, 18.7, 19.4, 21.1, 22.6, 22.8, 23.8, 24.3, 28.0, 28.2, 28.3, 31.9, 32.0, 35.8, 36.2, 36.9, 37.2, 39.0, 39.5, 39.8, 42.3, 50.2, 56.2, 56.8, 61.8, 67.2, 70.4, 70.6, 70.9, 72.5, 80.0, 121.6, 140.9. HR MS (FAB$^+$, $m$−NBA): calcd for $C_{33}H_{58}O_4Na$ ([M + Na]$^+$), 541.4233; found, 541.4229.

**Synthesis of 3.** Compound **2** (18.8 g, 36.3 mmol) was dissolved in a mixture of pyridine (60 mL) and chloroform (120 mL) in a 500 mL one-necked round-bottom flask. $p$-Toluenesulfonyl chloride (8.99 g, 47.1 mmol) was added to the stirred solution at 0 °C. The reaction mixture was stirred at 0 °C for 6 h and at room temperature for an additional 11 h. The solution was concentrated under reduced pressure, and the concentrate was poured onto water (400 mL). The crude product was recovered with EtOAc (400 mL × three times). The organic layer was dried over anhydrous $MgSO_4$, filtered, and concentrated under reduced pressure. Purification via silica gel column chromatography was performed by varying the eluent from EtOAc/hexane = 1:4 (v/v) to 100% EtOAc to increase its polarity. A pale yellow oil was obtained in an 83% yield. $R_f$ = 0.6 (EtOAc/hexane = 1:4, v/v). $^1$H NMR (300 MHz, $CDCl_3$) $\delta$ (ppm): 0.68 (s, 3H), 0.86 (dd, $J$ = 6.6, 1.2 Hz, 6H), 0.91 (d, $J$ = 6.6 Hz, 3H), 0.99 (s, 3H), 2.45 (s, 3H), 3.17 (m, 1H), 3.60 (m, 8H), 3.69 (t, $J$ = 4.8 Hz, 2H), 4.16 (t, $J$ = 4.8 Hz, 2H), 5.34 (d, $J$ = 5.4 Hz, 1H), 7.34 (d, $J$ = 8.4 Hz, 2H), 7.80 (d, $J$ = 8.1 Hz, 2H). $^{13}$C{$^1$H} NMR (126 MHz, $CDCl_3$) $\delta$ (ppm): 11.9, 18.7, 19.4, 21.1, 21.7, 22.6, 22.8, 23.8, 24.3, 28.0, 28.2, 28.4, 31.9, 32.0, 35.8, 36.2, 36.9, 37.2, 39.1, 39.5, 39.8, 42.3, 50.2, 56.2, 56.8, 67.3, 68.7, 69.2, 70.6, 70.8, 70.9, 79.5, 121.6, 128.0, 129.8, 133.0, 141.0, 144.8. MS (FAB$^+$, $m$−NBA): calcd for $C_{40}H_{65}O_6S$ ([M + H]$^+$), 673.45; found, 673.00.

**Synthesis of 4.** Compound **3** (14.0 g, 20.7 mmol) and 4-imidazolecarboxaldehyde (1.88 g, 19.5 mmol) were combined in a 500 mL one-necked round-bottom flask and dissolved in 180 mL of acetonitrile. After the addition of $K_2CO_3$ (3.51 g, 25.4 mmol), the reaction mixture was refluxed for 24 h. After it cooled to room temperature, the reaction mixture was poured onto water (300 mL) and neutralized by using 1.0 N HCl(aq). The crude product was extracted with $CH_2Cl_2$ (300 mL × three times). The organic layer was dried over anhydrous $MgSO_4$, filtered, and concentrated in vacuo. Silica gel column chromatography was performed by varying the eluent from EtOAc/$CH_3OH$ = 99:1 (v/v) to EtOAc/$CH_3OH$ = 9:1 (v/v) to increase its polarity. A pale yellow oil was isolated with a 48% yield. $R_f$ = 0.3 (EtOAc/$CH_3OH$ = 9:1, v/v). $^1$H NMR (300 MHz, $CDCl_3$) $\delta$ (ppm): 0.67 (s, 3H), 0.86 (dd, $J$ = 6.6, 1.2 Hz, 6H), 0.91 (d, $J$ = 6.6 Hz, 3H), 0.99 (s, 3H), 3.15 (m, 1H), 3.60 (m, 8H), 3.79 (t, $J$ = 5.1 Hz, 2H), 4.17 (t, $J$ = 5.1 Hz, 2H), 5.34 (d, $J$ = 5.1 Hz, 1H), 7.64 (d, $J$ = 1.2 Hz, 1H), 7.74 (d, $J$ = 1.2 Hz, 1H), 9.88 (s, 1H). $^{13}$C{$^1$H} NMR (126 MHz, $CDCl_3$) $\delta$ (ppm): 11.9, 18.7, 19.4, 21.1, 22.6, 22.8, 23.8, 24.3, 28.0, 28.2, 28.4, 29.7, 31.9, 31.94, 35.8, 36.2, 36.9, 37.2, 39.1, 39.5, 39.8, 42.3, 47.8, 56.1, 56.8, 67.3, 70.0, 70.6, 70.8, 71.0, 79.5, 121.6, 125.2, 139.2, 140.9, 142.3, 186.3. HR MS (FAB$^+$, $m$−NBA): calcd for $C_{37}H_{61}N_2O_4$ ([M + H]$^+$), 597.4631; found, 597.4636.

**Synthesis of 5.** Compound **4** (1.36 g, 2.28 mmol) and 2-picolylamine (0.246 g, 2.28 mmol) were dissolved in 16 mL of acetonitrile in a 50 mL one-necked round-bottom flask. A drop of acetic acid was added to the stirred solution, and the reaction mixture was refluxed for 7.5 h. After the mixture cooled to 0 °C, $NaBH_4$ (0.215 g, 5.70 mmol) was slowly added to the reaction mixture. The reaction mixture was stirred for an additional 22 h at room temperature. The reaction was quenched by adding 200 mL of water onto the solution, and the crude product was extracted with $CH_2Cl_2$ (200 mL × three times). The organic layer was dried over anhydrous $MgSO_4$, filtered, and concentrated under reduced pressure. Purification via silica gel column chromatography was performed by varying the eluent from $CH_2Cl_2$/$CH_3OH$ = 99:1 (v/v) to $CH_2Cl_2$/$CH_3OH$ = 9:1 (v/v) to increase its polarity. A yellow oil was isolated with a 10% yield. $R_f$ = 0.1 ($CH_2Cl_2$/$CH_3OH$ = 5:1, v/v). $^1$H NMR (300 MHz, $CDCl_3$) $\delta$ (ppm): 0.67 (s, 3H), 0.86 (dd, $J$ = 6.6, 1.2 Hz, 6H), 0.91 (d, $J$ = 6.6 Hz, 3H), 0.99 (s, 3H), 3.17 (m, 1H), 3.61 (m, 8H), 3.73 (t, $J$ = 5.1 Hz, 2H), 3.82 (s, 2H), 4.00 (s, 2H), 4.06 (t, $J$ = 5.1 Hz, 2H), 5.33 (d, $J$ = 5.1 Hz, 1H), 6.93 (s, 1H), 7.16 (m, 1H), 7.37 (d, $J$ = 7.8 Hz, 1H), 7.48 (d, $J$ = 1.2 Hz, 1H), 7.64 (td, $J$ = 7.8, 1.8 Hz, 1H), 8.55 (m, 1H). $^{13}$C{$^1$H} NMR (126 MHz, $CDCl_3$) $\delta$ (ppm): 11.9, 18.7, 19.4, 21.1, 22.6, 22.8, 23.8, 24.3, 28.0, 28.2, 28.4, 29.7, 31.9, 31.94, 35.8, 36.2, 36.9, 37.2, 39.1, 39.5, 39.8, 42.3, 46.7, 47.1, 50.2, 54.2, 56.2, 56.8, 67.3, 70.5, 70.6, 70.7, 71.0, 79.5, 117.1, 121.6, 122.0, 122.4, 136.5, 137.3, 140.2, 140.9, 149.2, 159.1. HR MS (FAB$^+$, $m$−NBA): calcd for $C_{43}H_{69}N_4O_3$ ([M + H]$^+$), 689.5370; found, 689.5364.

**Synthesis of 6.** A mixture of *trans*-chalcone (1.00 g, 4.80 mmol), nitromethane (1.30 mL, 24.0 mmol), and diethylamine (2.49 mL, 24.0 mmol) was added to a 10 mL one-necked round-bottom flask. The reaction mixture was heated at 60 °C for 7 h. After it cooled to room temperature, the reaction mixture was poured onto EtOAc (50 mL) and washed with brine (50 mL × twice). The organic layer was dried over anhydrous $MgSO_4$, filtered, and concentrated in vacuo. A pale yellow solid was obtained in a 98% yield and used in the next step without further purification. $R_f$ = 0.2 ($CH_2Cl_2$/hexane = 1:1, v/v). $^1$H NMR (300 MHz, $CDCl_3$) $\delta$ (ppm): 3.46 (dd, $J$ = 12.7, 7.5 Hz, 2H), 4.23 (tt, $J$ = 7.5, 6.9 Hz, 1H), 4.77 (dd, $J$ = 12.5, 6.9 Hz, 2H), 7.32 (m, 5H), 7.46 (m, 2H), 7.58 (m, 1H), 7.92 (m, 2H). $^{13}$C{$^1$H} NMR (126 MHz, $CDCl_3$) $\delta$ (ppm): 39.5, 41.7, 79.8, 124.8, 147.7, 128.1, 128.2, 128.9, 128.94, 129.3, 133.8, 136.6, 139.3, 197.0. HR MS (FAB$^+$, $m$−NBA): calcd for $C_{16}H_{16}NO_3$ ([M + H]$^+$), 270.1130; found, 270.1131.

**Synthesis of 7.** Compound **6** (0.500 g, 1.86 mmol) was dissolved in 10 mL of $CF_3CH_2OH$ in a 50 mL one-necked round-bottom flask. $NH_4OAc$ (8.82 g, 114 mmol) was added to a stirred solution of the reaction mixture, and the solution was refluxed for 2 h. The reaction mixture was cooled to room temperature and poured onto $CH_2Cl_2$ (300 mL). The organic solution was washed with water (300 mL × three times), 1 M NaOH(aq) (300 mL), and water (300 mL). The organic layer was dried over anhydrous $MgSO_4$, filtered, and concentrated under reduced pressure. Silica gel column chromatography was performed by varying the eluent from $CH_2Cl_2$/hexane = 1:1 (v/v) to 100% $CH_2Cl_2$ to increase its polarity. A black solid was obtained in a 42% yield. $R_f$ = 0.6 ($CH_2Cl_2$/hexane = 1:1, v/v). $^1$H NMR (300 MHz, $CDCl_3$) $\delta$ (ppm): 7.21 (s, 2H), 7.46 (m, 12H), 7.97 (m, 4H), 8.07 (m, 4H). $^{13}$C{$^1$H} NMR (126 MHz, $CDCl_3$) $\delta$ (ppm): 115.1, 126.8, 128.2, 128.5, 129.3, 129.4, 130.3, 132.4, 133.9, 142.8, 149.8, 155.3. HR MS (FAB$^+$, $m$−NBA): calcd for $C_{32}H_{24}N_3$ ([M + H]$^+$), 450.1970; found, 450.1966.

**Synthesis of 8.** Compound **7** (0.150 g, 0.334 mmol) was diluted in triethylamine (0.820 mL) in a 10 mL one-necked round-bottom flask. $BF_3$·$OEt_2$ (0.810 mL, 6.75 mmol) was carefully added into the stirred solution. After it was heated at 90 °C for 5 h, the solution was cooled to room temperature. The reaction mixture was poured onto $CH_2Cl_2$ (150 mL) and washed with 1 M HCl(aq) (150 mL) and brine (150 mL × twice). The organic layer was dried over anhydrous $MgSO_4$, filtered, and concentrated in vacuo. Purification via silica gel column chromatography was performed with varying the eluent from hexane to $CH_2Cl_2$/hexane = 1:1 (v/v) to increase its polarity. A black solid was isolated in a 44% yield. $R_f$ = 0.4 ($CH_2Cl_2$/hexane = 1:1, v/v). $^1$H NMR (300 MHz, $CDCl_3$) $\delta$ (ppm): 7.05 (s, 2H), 7.47 (m, 12H), 8.06 (m, 8H). $^{13}$C{$^1$H} NMR (126 MHz, $CDCl_3$) $\delta$ (ppm): 119.3, 128.8, 128.9, 129.6, 129.7, 129.8, 129.8, 131.1, 131.8, 132.5, 144.4, 145.8, 159.8. HR MS (FAB$^+$, $m$−NBA): calcd for $C_{32}H_{22}BF_2N_3$ ([M$^+$]), 497.1875; found, 497.1880.

**Synthesis of 9.** $POCl_3$ (7.30 mL, 78.3 mmol) was slowly added into anhydrous DMF (7.30 mL, 94.9 mmol) in a 50 mL two-necked round-bottom flask under an Ar atmosphere at 0 °C. The reaction mixture was stirred at 0 °C for 5 min and then at room temperature for 30 min. Compound **8** (110 mg, 0.220 mmol) dissolved in $CH_2Cl_2$ (8.0 mL) was added slowly into the stirred solution which was heated at 70 °C for 6 h. The reaction was quenched by adding saturated $NaHCO_3$(aq) (100 mL) at 0 °C. The crude product was extracted


https://dx.doi.org/10.1021/acs.inorgchem.0c01376
Inorg. Chem. XXXX, XXX, XXX−XXX

with $CH_2Cl_2$ (200 mL × three times). The recovered organic layer was dried over anhydrous $MgSO_4$, filtered, and concentrated under reduced pressure. Purification via silica gel column chromatography was performed with varying the eluent from EtOAc/hexane = 1:19 (v/v) to EtOAc/hexane = 1:2 (v/v) to increase its polarity. Dark blue powders were obtained with a 51% yield. $R_f$ = 0.3 (EtOAc/hexane = 1:2, v/v). $^1$H NMR (300 MHz, $CDCl_3$) $\delta$ (ppm): 7.25 (s, 1H), 7.54 (m, 12H), 7.75 (m, 2H), 7.88 (m, 2H), 8.10 (m, 4H), 9.80 (s, 1H). $^{13}C\{^1H\}$ NMR (126 MHz, $CDCl_3$) $\delta$ (ppm): 121.7, 125.8, 127.9, 128.0, 128.2, 128.4, 128.5, 129.1, 129.2, 129.4, 129.8, 128.9, 130.0, 130.4, 130.5, 130.9, 131.0, 131.1, 132.2, 133.0, 143.4, 147.7, 149.0, 159.6, 166.5, 186.4. HR MS (FAB$^+$, *m*−NBA): calcd for $C_{33}H_{23}BF_2N_3O$ ([M + H]$^+$), 526.1902; found, 526.1904.

**Synthesis of JJ.** Compounds **5** (0.110 g, 0.160 mmol) and **9** (0.060 g, 0.114 mmol) were dissolved in 12 mL of anhydrous $CH_2Cl_2$ in a 25 mL two-necked round-bottom flask. $NaBH(OAc)_3$ (0.041 g, 0.193 mmol) was then added into the stirred solution. After the addition of a drop of acetic acid, the reaction mixture was refluxed for 48 h. The solution was cooled to room temperature and poured onto water (100 mL). The crude product was extracted with $CH_2Cl_2$ (100 mL × three times). The recovered organic layer was dried over anhydrous $MgSO_4$, filtered, and concentrated under reduced pressure. Preparative TLC techniques were employed with $CH_2Cl_2/CH_3OH$ = 5:1 (v/v) as the eluent to purify JJ. A black solid was isolated in a 12% yield. $R_f$ = 0.3 ($CH_2Cl_2/CH_3OH$ = 5:1, v/v). $^1$H NMR (300 MHz, $CD_3CN$) $\delta$ (ppm): 0.58 (s, 3H), 0.86 (m, 12H), 2.99 (m, 1H), 3.28 (s, 2H), 3.45 (m, 10H), 3.64 (t, *J* = 4.8 Hz, 2H), 3.71 (s, 2H), 3.98 (t, *J* = 4.8 Hz, 2H), 5.21 (d, *J* = 5.1 Hz, 1H), 6.91 (d, *J* = 7.8 Hz, 1H), 7.10 (m, 1H), 7.22 (s, 1H), 7.53 (m, 15H), 7.65 (d, *J* = 7.2 Hz, 2H), 7.80 (m, 2H), 7.95 (dd, *J* = 7.2, 1.8 Hz, 2H), 8.08 (m, 2H), 8.36 (d, *J* = 3.6 Hz, 1H). $^{13}C\{^1H\}$ NMR (126 MHz, $CDCl_3$) $\delta$ (ppm): 13.1, 14.3, 18.9, 19.6, 21.3, 22.8, 22.9, 23.0, 24.0, 24.5, 25.0, 27.4, 28.2, 28.4, 28.6, 29.3, 29.5, 29.6, 29.7, 29.8, 29.9, 32.1, 33.7, 36.0, 36.4, 37.1, 37.4, 39.3, 39.7, 40.0, 42.5, 50.4, 56.4, 57.0, 67.5, 70.8, 70.9, 71.2, 79.7, 121.8, 128.1, 128.4, 128.8, 129.4, 129.7, 130.1, 130.2, 131.2, 136.7, 141.1, 148.6. HR MS (FAB$^+$, *m*−NBA): calcd for $C_{76}H_{91}BF_2N_7O_3$ ([M + H]$^+$), 1198.7245; found, 1198.7244.

**Synthesis of 10.** 2-Bromoethyl ethyl ether (2.85 g, 17.7 mmol) and 4-imidazolecarboxaldehyde (1.00 g, 10.4 mmol) were dissolved in 100 mL of acetonitrile in a 250 mL one-necked round-bottom flask. $K_2CO_3$ (2.16 g, 15.6 mmol) was delivered into the stirred solution, which was then refluxed for 26 h. The reaction mixture was cooled to room temperature and was poured onto water (300 mL). The crude product was extracted with $CH_2Cl_2$ (300 mL × three times). The recovered organic layer was dried over anhydrous $MgSO_4$, filtered, and concentrated in vacuo. Silica gel column chromatography was performed with varying the eluent from $CH_2Cl_2/CH_3OH$ = 99:1 (v/v) to $CH_2Cl_2/CH_3OH$ = 49:1 (v/v) to increase its polarity, which afforded a pale yellow oil in a 57% yield. $R_f$ = 0.3 ($CH_2Cl_2/CH_3OH$ = 9:1, v/v). $^1$H NMR (300 MHz, $CDCl_3$) $\delta$ (ppm): 1.19 (t, *J* = 6.9 Hz, 3H), 3.49 (q, *J* = 6.9 Hz, 2H), 3.69 (t, *J* = 4.8 Hz, 2H), 4.15 (t, *J* = 4.8 Hz, 2H), 7.62 (d, *J* = 0.9 Hz, 1H), 7.71 (d, *J* = 0.9 Hz, 1H), 9.88 (s, 1H). $^{13}C\{^1H\}$ NMR (126 MHz, $CDCl_3$) $\delta$ (ppm): 15.0, 47.9, 66.9, 69.1, 125.2, 139.2, 142.3, 186.3. HR MS (FAB$^+$, *m*−NBA): calcd for $C_8H_{13}N_2O_2$ ([M + H]$^+$), 169.0977; found, 169.0977.

**Synthesis of 11.** A method identical to the synthetic procedure for compound **5** was employed, except that compound **10** (0.600 g, 3.57 mmol) was used instead of compound **4**. A pale brown oil was obtained in a 16% yield. $R_f$ = 0.1 ($CH_2Cl_2/CH_3OH$ = 5:1, v/v). $^1$H NMR (300 MHz, $CDCl_3$) $\delta$ (ppm): 1.18 (t, *J* = 6.9 Hz, 3H), 3.47 (q, *J* = 6.9 Hz, 2H), 3.65 (t, *J* = 5.4 Hz, 2H), 3.82 (s, 2H), 4.00 (s, 2H), 4.04 (t, *J* = 5.1 Hz, 2H), 6.92 (s, 1H), 7.15 (m, 1H), 7.37 (d, *J* = 7.8 Hz, 1H), 7.47 (d, *J* = 1.2 Hz, 1H), 7.64 (td, *J* = 7.8, 1.8 Hz, 2H), 8.55 (m, 1H). $^{13}C\{^1H\}$ NMR (126 MHz, $CDCl_3$) $\delta$ (ppm): 15.0, 46.7, 47.2, 54.4, 66.8, 69.7, 116.9, 121.9, 122.3, 136.5, 137.2, 140.5, 149.2, 159.5. HR MS (FAB$^+$, *m*−NBA): calcd for $C_{14}H_{21}N_4O$ ([M + H]$^+$), 261.1715; found, 261.1716.

**Synthesis of JJC.** A method identical to the synthetic procedure for JJ was employed, except that compound **11** (0.092 g, 0.353 mmol) was used instead of compound **5**. A dark blue solid was obtained in a 31% yield. $R_f$ = 0.2 ($CH_2Cl_2/CH_3OH$ = 5:1, v/v). $^1$H NMR (300 MHz, $CD_2Cl_2$) $\delta$ (ppm): 1.04 (t, *J* = 6.9 Hz, 3H), 3.20 (s, 2H), 3.33 (q, *J* = 6.9 Hz, 2H), 3.36 (s, 2H), 3.48 (t, *J* = 5.1 Hz, 2H), 3.64 (s, 2H), 3.85 (t, *J* = 5.1 Hz, 2H), 7.58 (d, *J* = 6.3 Hz, 2H), 7.71 (m, 2H), 7.85 (m, 2H), 7.95 (m, 2H), 8.27 (d, *J* = 3.6 Hz, 1H). $^{13}C\{^1H\}$ NMR (126 MHz, $CD_2Cl_2$) $\delta$ (ppm): 15.4, 47.8, 48.6, 51.2, 59.5, 67.1, 70.0, 118.6, 119.5, 122.1, 123.4, 126.7, 128.3, 128.5, 128.7, 129.0, 129.1, 129.3, 129.6, 129.7, 130.1, 130.2, 131.4, 131.8, 132.0, 132.1, 132.6, 132.8, 136.6, 137.0, 138.4, 144.7, 145.1, 145.3, 148.9, 160.3, 161.4. HR MS (FAB$^+$, *m*−NBA): calcd for $C_{47}H_{43}BF_2N_7O$ ([M + H]$^+$), 770.3590; found, 770.3594.

*Caution*: Perchlorate salts are potentially explosive. Only small amounts of materials should be cautiously handled at a time.

**Spectroscopic Measurements.** Milli-Q grade water (18.2 MΩ·cm) was used to prepare the solutions for spectroscopic measurements. PIPES (piperazine-*N*,*N*′-bis(2-ethanesulfonic acid), ≥99%) was purchased from Aldrich. A pH 7.4 buffer solution was prepared by dissolving PIPES (25 mM) and KCl (100 mM) in Milli-Q water and adjusting the pH with standard KOH solution (45 wt %, Aldrich) or concentrated HCl (Aldrich). The buffer solution was further treated with Chelex 100 resin (BIO-RAD) to remove trace metal ions and filtered through a membrane (pore size = 0.45 μm); its pH was confirmed prior to use. Fresh metal stock solutions (typically, 0.10 or 0.010 M except for $CrCl_3·6H_2O$) were prepared in Milli-Q water by using the corresponding chloride salts: $CuCl_2$ (99.999%, Aldrich), NaCl (≥99.5%, Aldrich), KCl (Puratronic grade, Calbiochem), $MgCl_2$ (99.99%, Aldrich), $CaCl_2$ (99.99%, Aldrich), $CrCl_3·6H_2O$ (98%, Aldrich), $MnCl_2$ (99.99%, Aldrich), $FeCl_2$ (99.99%, Aldrich), $CoCl_2$ (99.9%, Aldrich), $NiCl_2$ (99.99%, Aldrich), $CdCl_2$ (99.99%, Aldrich), and $ZnCl_2$ (99.999%, Aldrich). A TPEN solution was prepared by dissolving *N*,*N*,*N*′,*N*′-tetrakis(2-picolyl)ethylenediamine (≥99%, Sigma) in DMSO (99.9%, Aldrich). $Zn(ClO_4)_2·6H_2O$ (Aldrich) was dissolved in $CH_3CN$ (spectrophotometric grade, Aldrich) at concentrations of 1.0, 10, and 100 mM. Sensor solutions were prepared by dissolution in DMSO at a concentration of 10 mM and were partitioned into Eppendorf tubes. The sensor stock solution was stored in a refrigerator at −10 °C and were thawed before the measurements. Typically, 3.0 mL of the buffer and 3 μL of the sensor stock solution (10 mM in DMSO) were mixed to give a 10 μM solution. A 1 cm × 1 cm fluorimeter cell (Hellma) was used in the steady-state photophysical measurements. UV−vis absorption spectra were collected on a Varian Cary 300 spectrophotometer at room temperature. Photoluminescence spectra were obtained by using a Quanta Master 400 scanning spectrofluorimeter at room temperature. The photoluminescence quantum yields ($\Phi$) were relatively determined according to following standard equation: $\Phi = \Phi_{ref} \times (I/I_{ref}) \times (A_{ref}/A) \times (n/n_{ref})^2$, where *A*, *I*, and *n* are the absorbance at the excitation wavelength, the integrated photoluminescence intensity, and the refractive index of the solvent, respectively. 9,10-Diphenylanthracene in a deaerated toluene solution was used as the external reference ($\Phi_{ref}$ = 1.00).[85]

**Transient Photoluminescence Measurements.** Photoluminescence decay traces were acquired based on time-correlated single-photon counting (TCSPC) techniques by using a FluoTime 200 instrument (PicoQuant, Germany). A 377 nm diode laser (PicoQuant, Germany; pulse energy = 35 pJ) with a repetition rate of 125 kHz was used as the excitation source. The signals at 654 and 652 nm were obtained by using an automated motorized monochromator and recorded with a NanoHarp unit. The decay profiles were analyzed (OriginPro 8.0, OriginLab) by using single or double exponential decay models.

**Electrochemical Characterization.** Cyclic and differential pulse voltammetry measurements were carried out by using a CH Instruments, CHI630 B potentiostat with a three-electrode-cell assembly. A Pt wire and a Pt microdisc were used as the counter electrode and the working electrode, respectively. An $Ag/AgNO_3$ (10 mM) couple was used as the pseudo reference electrode. Measurements were carried out in Ar-saturated THF/DMSO (4:1, v/v) with using 0.10 M tetra-*n*-butylammonium hexafluorophosphate ($TBAPF_6$) as the supporting electrolyte at scan rates of 0.1 mV s$^{-1}$


https://dx.doi.org/10.1021/acs.inorgchem.0c01376
Inorg. Chem. XXXX, XXX, XXX−XXX

(cyclic voltammetry) and 4.0 mV $s^{-1}$ (differential pulse voltammetry). A ferrocenium/ferrocene ($Fc^+$/Fc) couple was employed as the external reference.

**Determination of $K_d$.** Zinc-buffered solutions (pH 7.4; 100 mM HEPES, 100 mM $NaNO_3$, and 10 mM HEDTA) were employed to determine the dissociation constant ($K_d$). The procedure reported by Nagano and co-workers was modified to prepare 15 solutions of free zinc with concentrations in the range 0.15 pM to 120 nM.[94] A 1.5 $\mu$L sensor solution (10 mM, DMSO) was added to each zinc-buffered solution (3 mL), which was then stored for at least 3 h. The fluorescence spectrum of each solution was recorded and the intensity was calculated by integrating the spectrum from 550 to 850 nm. A zinc binding titration isotherm plotting the fluorescence intensity as a function of the free zinc concentration was constructed and fitted to a 1:1 binding equation.[94]

**Cell Cultures.** HeLa and DLD-1 cells were obtained from Korean Cell Line Bank and cultured in DMEM supplemented with 10% fetal bovine serum and 1% penicillin/streptomycin at 37 °C in a humidified incubator under 5% $CO_2$. Two days before imaging, cells were passed and plated onto poly(D-lysine)-coated glass-bottom culture dishes.

**Confocal Laser Scanning Microscopy.** Microscopic experiments were performed at the Korea Basic Science Institute, Seoul, Korea. Sensor solutions were prepared by dissolving 10 mM stock solution (DMSO) in serum-free DMEM. A 100 mM $ZnCl_2$(aq) solution was prepared in Milli-Q grade water. A 100 mM sodium pyrithione solution was prepared in DMSO, prior to the microscopic experiments. Serum-free DMEM solutions containing 200 $\mu$M EDTA were also prepared. Typically, after washing the cells with PBS, medium containing 0.2 $\mu$M sensor was added to a culture dish. The cells were incubated for 10 min at 37 °C. The incubated cells were washed with PBS and fresh DMEM (serum-free), and fluorescence micrographs were obtained by using a Carl Zeiss LSM 510 META confocal laser scanning microscope with a Newport MaiTai eHP DeepSee multiphoton excitation system. An excitation beam (633 nm) was focused onto the dish, and the signals were acquired through 32 emission channels covering the range 640−677 nm. After removing the cell medium, the cells were washed with fresh DMEM and incubated in DMEM containing 20 $\mu$M $ZnCl_2$ for 5 min. The cells were imaged after washing with FBS and supplemented with fresh DMEM. Finally, the cells were treated with 200 $\mu$M EDTA, and microscopic visualization was performed. Photoluminescence images and mean intensities were processed by using the software ZEN2000 and ImageJ, respectively.

## ■ ASSOCIATED CONTENT

### Supporting Information

The Supporting Information is available free of charge at https://pubs.acs.org/doi/10.1021/acs.inorgchem.0c01376.

(Table S1) Photophysical parameters of JJ; (Scheme S1) synthesis of JJC; (Figures S1−S38) fluorescence zinc responses of JJ in aqueous buffers containing 66 vol % DMSO, UV−vis absorption and fluorescence spectra of JJ and JJC obtained in the absence and presence of zinc ions in $CH_3CN$, fluorescence decay traces of JJ and JJC in the absence and presence of zinc ions, fluorescence Job plots, the zinc and pH titration isotherms of JJC, fluorescence selectivity of JJC toward zinc binding, intracellular localization of JJC in HeLa cells, intracellular uptake of JJ, visualization of intracellular zinc in DLD-1 cells, and $^1H$ and $^{13}C\{^1H\}$ NMR spectra (PDF)

Movie S1 (MP4)

## ■ AUTHOR INFORMATION


### Corresponding Author

**Youngmin You** − *Division of Chemical Engineering and Materials Science, Ewha Womans University, Seoul 03760, Republic of Korea;* orcid.org/0000-0001-5633-6599; Email: odds2@ewha.ac.kr

### Authors

**Jin Ju Kim** − *Division of Chemical Engineering and Materials Science, Ewha Womans University, Seoul 03760, Republic of Korea*

**Jayeon Hong** − *Division of Chemical Engineering and Materials Science, Ewha Womans University, Seoul 03760, Republic of Korea*

**Seungyeon Yu** − *Division of Chemical Engineering and Materials Science, Ewha Womans University, Seoul 03760, Republic of Korea*

Complete contact information is available at: https://pubs.acs.org/10.1021/acs.inorgchem.0c01376

### Author Contributions

†These authors contributed equally to this work.


### Notes

The authors declare no competing financial interest.

## ■ ACKNOWLEDGMENTS

This work was supported by the Ministry of Science, Information, and Communication Technology (ICT) and Future Planning (MSIP) of Korea through the GFP grant (CISS-2012M3A6A6054204) and by the Midcareer Research Program (NRF2019R1A2C2003969) through the National Research Foundation grant. The authors thank Dr. Seung-Hae Kwon at the Korea Basic Science Institute for the assistance with the microscopic experiments.

## ■ REFERENCES


(1) Frederickson, C. J.; Koh, J.-Y.; Bush, A. I. The neurobiology of zinc in health and disease. *Nat. Rev. Neurosci.* **2005**, *6*, 449−462.

(2) Sladek, R.; Rocheleau, G.; Rung, J.; Dina, C.; Shen, L.; Serre, D.; Boutin, P.; Vincent, D.; Belisle, A.; Hadjadj, S.; Balkau, B.; Heude, B.; Charpentier, G.; Hudson, T. J.; Montpetit, A.; Pshezhetsky, A. V.; Prentki, M.; Posner, B. I.; Balding, D. J.; Meyre, D.; Polychronakos, C.; Froguel, P. A genome-wide association study identifies novel risk loci for type 2 diabetes. *Nature* **2007**, *445*, 881−885.

(3) Walker, C. L. F.; Bhutta, Z. A.; Bhandari, N.; Teka, T.; Shahid, F.; Taneja, S.; Black, R. E. Zinc during and in convalescence from diarrhea has no demonstrable effect on subsequent morbidity and anthropometric status among infants 6 mo of age. *Am. J. Clin. Nutr.* **2007**, *85*, 887−894.

(4) Taylor, C. G. Zinc, the pancreas, and diabetes: insights from rodent studies and future directions. *BioMetals* **2005**, *18*, 305−312.

(5) Maret, W.; Krezel, A. Cellular zinc and redox buffering capacity of metallothionein/thionein in health and disease. *Mol. Med.* **2007**, *13*, 371−375.

(6) Suhy, D. A.; Simon, K. D.; Linzer, D. I. H.; O'Halloran, T. V. Metallothionein is part of a zinc-scavenging mechanism for cell survival under conditions of extreme zinc deprivation. *J. Biol. Chem.* **1999**, *274*, 9183−9192.

(7) Colvin, R. A.; Holmes, W. R.; Fontaine, C. P.; Maret, W. Cytosolic zinc buffering and muffling: their role in intracellular zinc homeostasis. *Metallomics* **2010**, *2*, 306−317.

(8) Sensi, S. L.; Paoletti, P.; Bush, A. I.; Sekler, I. Zinc in the physiology and pathology of the CNS. *Nat. Rev. Neurosci.* **2009**, *10*, 780−791.

(9) Sensi, S. L.; Paoletti, P.; Koh, J.-Y.; Aizenman, E.; Bush, A. I.; Hershfinkel, M. The neurophysiology and pathology of brain zinc. *J. Neurosci.* **2011**, *31*, 16076−16085.
(10) Choi, D. W.; Koh, J. Y. Zinc and brain injury. *Annu. Rev. Neurosci.* **1998**, *21*, 347−375.
(11) Walker, C. F.; Black, R. E. Zinc and the risk for infectious disease. *Annu. Rev. Nutr.* **2004**, *24*, 255−275.
(12) Chasapis, C. T.; Loutsidou, A. C.; Spiliopoulou, C. A.; Stefanidou, M. E. Zinc and human health: an update. *Arch. Toxicol.* **2012**, *86*, 521−534.
(13) Bleackley, M. R.; MacGillivray, R. T. A. Transition metal homeostasis: from yeast to human disease. *BioMetals* **2011**, *24*, 785−809.
(14) Frederickson, C. J.; Bush, A. I. Synaptically released zinc: physiological functions and pathological effects. *BioMetals* **2001**, *14*, 353−366.
(15) Suh, S. W.; Jensen, K. B.; Jensen, M. S.; Silva, D. S.; Kesslak, P. J.; Danscher, G.; Frederickson, C. J. Histochemically-reactive zinc in amyloid plaques, angiopathy, and degenerating neurons of Alzheimer's diseased brains. *Brain Res.* **2000**, *852*, 274−278.
(16) Berni Canani, R.; Buccigrossi, V.; Passariello, A. Mechanisms of action of zinc in acute diarrhea. *Curr. Opin. Gastroenterol.* **2011**, *27*, 8−12.
(17) Weiss, J. H.; Sensi, S. L.; Koh, J. Y. $Zn^{2+}$: a novel ionic mediator of neural injury in brain disease. *Trends Pharmacol. Sci.* **2000**, *21*, 395−401.
(18) Bush, A. I.; Pettingell, W. H.; Multhaup, G.; Paradis, M. d.; Vonsattel, J.-P.; Gusella, J. F.; Beyreuther, K.; Masters, C. L.; Tanzi, R. E. Rapid induction of Alzheimer A$\beta$ amyloid formation by zinc. *Science* **1994**, *265*, 1464−1467.
(19) Lee, J.-Y.; Cole, T. B.; Palmiter, R. D.; Suh, S. W.; Koh, J.-Y. Contribution by synaptic zinc to the gender-disparate plaque formation in human Swedish mutant APP transgenic mice. *Proc. Natl. Acad. Sci. U. S. A.* **2002**, *99*, 7705−7710.
(20) Costello, L. C.; Franklin, R. B. The clinical relevance of the metabolism of prostate cancer; zinc and tumor suppression: connecting the dots. *Mol. Cancer* **2006**, *5*, 17.
(21) Prasad, A. S. Zinc in human health: effect of zinc on immune cells. *Mol. Med.* **2008**, *14*, 353−357.
(22) Koh, J.-Y.; Suh, S. W.; Gwag, B. J.; He, Y. Y.; Hsu, C. Y.; Choi, D. W. The role of zinc in selective neuronal death after transient global cerebral ischemia. *Science* **1996**, *272*, 1013−1016.
(23) Mocchegiani, E.; Bertoni-Freddari, C.; Marcellini, F.; Malavolta, M. Brain, aging and neurodegeneration: role of zinc ion availability. *Prog. Neurobiol.* **2005**, *75*, 367−390.
(24) Toth, K. Zinc in neurotransmission. *Annu. Rev. Nutr.* **2011**, *31*, 139−153.
(25) Takeda, A. Zinc homeostasis and functions of zinc in the brain. *BioMetals* **2001**, *14*, 343−351.
(26) Jo, S. M.; Won, M. H.; Cole, T. B.; Jensen, M. S.; Palmiter, R. D.; Danscher, G. Zinc-enriched (ZEN) terminals in mouse olfactory bulb. *Brain Res.* **2000**, *865*, 227−236.
(27) Li, Y.; Hough, C. J.; Frederickson, C. J.; Sarvey, J. M. Induction of mossy fiber→CA3 long-term potentiation requires translocation of synaptically released $Zn^{2+}$. *J. Neurosci.* **2001**, *21*, 8015−8025.
(28) Huang, E. P. Metal ions and synaptic transmission: think zinc. *Proc. Natl. Acad. Sci. U. S. A.* **1997**, *94*, 13386−13387.
(29) Vogt, K.; Mellor, J.; Tong, G.; Nicoll, R. The actions of synaptically released zinc at hippocampal mossy fiber synapses. *Neuron* **2000**, *26*, 187−196.
(30) Kay, A. R.; Neyton, J.; Paoletti, P. A startling role for synaptic zinc. *Neuron* **2006**, *52*, 572−574.
(31) Bonaventura, P.; Benedetti, G.; Albarede, F.; Miossec, P. Zinc and its role in immunity and inflammation. *Autoimmun. Rev.* **2015**, *14*, 277−285.
(32) Yamasaki, S.; Sakata-Sogawa, K.; Hasegawa, A.; Suzuki, T.; Kabu, K.; Sato, E.; Kurosaki, T.; Yamashita, S.; Tokunaga, M.; Nishida, K.; Hirano, T. Zinc is a novel intracellular second messenger. *J. Cell Biol.* **2007**, *177*, 637−645.
(33) Flinn, J. M.; Hunter, D.; Linkous, D. H.; Lanzirotti, A.; Smith, L. N.; Brightwell, J.; Jones, B. F. Enhanced zinc consumption causes memory deficits and increased brain levels of zinc. *Physiol. Behav.* **2005**, *83*, 793−803.
(34) Blanchard, R. K.; Moore, J. B.; Green, C. L.; Cousins, R. J. Modulation of intestinal gene expression by dietary zinc status: effectiveness of cDNA arrays for expression profiling of a single nutrient deficiency. *Proc. Natl. Acad. Sci. U. S. A.* **2001**, *98*, 13507−13513.
(35) Jackson, K. A.; Valentine, R. A.; Coneyworth, L. J.; Mathers, J. C.; Ford, D. Mechanisms of mammalian zinc-regulated gene expression. *Biochem. Soc. Trans.* **2008**, *36*, 1262−1266.
(36) Truong-Tran, A. Q.; Carter, J.; Ruffin, R. E.; Zalewski, P. D. The role of zinc in caspase activation and apoptotic cell death. *BioMetals* **2001**, *14*, 315−330.
(37) Franklin, R. B.; Costello, L. C. The important role of the apoptotic effects of zinc in the development of cancers. *J. Cell. Biochem.* **2009**, *106*, 750−757.
(38) Kimura, E.; Aoki, S.; Kikuta, E.; Koike, T. A macrocyclic zinc(II) fluorophore as a detector of apoptosis. *Proc. Natl. Acad. Sci. U. S. A.* **2003**, *100*, 3731−3736.
(39) Beyersmann, D.; Haase, H. Functions of zinc in signaling, proliferation and differentiation of mammalian cells. *BioMetals* **2001**, *14*, 331−341.
(40) Yamaguchi, S.; Miura, C.; Kikuchi, K.; Celino, F. T.; Agusa, T.; Tanabe, S.; Miura, T. Zinc is an essential trace element for spermatogenesis. *Proc. Natl. Acad. Sci. U. S. A.* **2009**, *106*, 10859−10864.
(41) Oteiza, P. I. Zinc and the modulation of redox homeostasis. *Free Radical Biol. Med.* **2012**, *53*, 1748−1759.
(42) Nolan, E. M.; Lippard, S. J. Small-molecule fluorescent sensors for investigating zinc metalloneurochemistry. *Acc. Chem. Res.* **2009**, *42*, 193−203.
(43) Lim, N. C.; Freake, H. C.; Brückner, C. Illuminating zinc in biological systems. *Chem. - Eur. J.* **2005**, *11*, 38−49.
(44) Carter, K. P.; Young, A. M.; Palmer, A. E. Fluorescent sensors for measuring metal ions in living systems. *Chem. Rev.* **2014**, *114*, 4564−4601.
(45) Chen, Y.; Bai, Y.; Han, Z.; He, W.; Guo, Z. Photoluminescence imaging of $Zn^{2+}$ in living systems. *Chem. Soc. Rev.* **2015**, *44*, 4517−4546.
(46) Kimura, E.; Koike, T. Recent development of zinc-fluorophores. *Chem. Soc. Rev.* **1998**, *27*, 179−184.
(47) Xu, Z.; Yoon, J.; Spring, D. R. Fluorescent chemosensors for $Zn^{2+}$. *Chem. Soc. Rev.* **2010**, *39*, 1996−2006.
(48) Jiang, P.; Guo, Z. Fluorescent detection of zinc in biological systems: recent development on the design of chemosensors and biosensors. *Coord. Chem. Rev.* **2004**, *248*, 205−229.
(49) Trusso Sfrazzetto, G.; Satriano, C.; Tomaselli, G. A.; Rizzarelli, E. Synthetic fluorescent probes to map metallostasis and intracellularfate of zinc and copper. *Coord. Chem. Rev.* **2016**, *311*, 125−167.
(50) Tomat, E.; Lippard, S. J. Imaging mobile zinc in biology. *Curr. Opin. Chem. Biol.* **2010**, *14*, 225−230.
(51) Frederickson, C. J.; Kasarskis, E. J.; Ringo, D.; Frederickson, R. E. A quinoline fluorescence method for visualizing and assaying the histochemically reactive zinc (bouton zinc) in the brain. *J. Neurosci. Methods* **1987**, *20*, 91−103.
(52) Huang, Z.; Lippard, S. J. Illuminating mobile zinc with fluorescence: from cuvettes to live cells and tissues. *Methods Enzymol.* **2012**, *505*, 445−468.
(53) Dai, Z.; Canary, J. W. Tailoring tripodal ligands for zinc sensing. *New J. Chem.* **2007**, *31*, 1708−1718.
(54) Pluth, M. D.; Tomat, E.; Lippard, S. J. Biochemistry of mobile zinc and nitric oxide revealed by fluorescent sensors. *Annu. Rev. Biochem.* **2011**, *80*, 333−355.
(55) Que, E. L.; Domaille, D. W.; Chang, C. J. Metals in neurobiology: probing their chemistry and biology with molecular imaging. *Chem. Rev.* **2008**, *108*, 1517−1549.


https://dx.doi.org/10.1021/acs.inorgchem.0c01376
Inorg. Chem. XXXX, XXX, XXX−XXX

(56) Masanta, G.; Lim, C. S.; Kim, H. J.; Han, J. H.; Kim, H. M.; Cho, B. R. A mitochondrial-targeted two-photon probe for zinc ion. *J. Am. Chem. Soc.* **2011**, *133*, 5698−5700.
(57) Xue, L.; Li, G.; Yu, C.; Jiang, H. A ratiometric and targetable fluorescent sensor for quantification of mitochondrial zinc ions. *Chem. - Eur. J.* **2012**, *18*, 1050−1054.
(58) Liu, Z.; Zhang, C.; Chen, Y.; He, W.; Guo, Z. An excitation ratiometric $Zn^{2+}$ sensor with mitochondria-targetability for monitoring of mitochondrial $Zn^{2+}$ release upon different stimulations. *Chem. Commun.* **2012**, *48*, 8365−8367.
(59) Chyan, W.; Zhang, D. Y.; Lippard, S. J.; Radford, R. J. Reaction-based fluorescent sensor for investigating mobile $Zn^{2+}$ in mitochondria of healthy versus cancerous prostate cells. *Proc. Natl. Acad. Sci. U. S. A.* **2014**, *111*, 143−148.
(60) Fang, L.; Trigiante, G.; Crespo-Otero, R.; Philpott, M. P.; Jones, C. R.; Watkinson, M. An alternative modular 'click-$S_N$Ar-click' approach to develop subcellular localized fluorescent probes to image mobile $Zn^{2+}$. *Org. Biomol. Chem.* **2019**, *17*, 10013−10019.
(61) Xue, L.; Li, G.; Zhu, D.; Liu, Q.; Jiang, H. Rational design of a ratiometric and targetable fluorescent probe for imaging lysosomal zinc ions. *Inorg. Chem.* **2012**, *51*, 10842−10849.
(62) Zhu, H.; Fan, J.; Zhang, S.; Cao, J.; Song, K.; Ge, D.; Dong, H.; Wang, J.; Peng, X. Ratiometric fluorescence imaging of lysosomal $Zn^{2+}$ release under oxidative stress in neural stem cells. *Biomater. Sci.* **2014**, *2*, 89−97.
(63) Lee, H.-J.; Cho, C.-W.; Seo, H.; Singha, S.; Jun, Y. W.; Lee, K.-H.; Jung, Y.; Kim, K.-T.; Park, S.; Bae, S. C.; Ahn, K. H. A two-photon fluorescent probe for lysosomal zinc ions. *Chem. Commun.* **2016**, *52*, 124−127.
(64) Du, C.; Fu, S.; Wang, X.; Sedgwick, A. C.; Zhen, W.; Li, M.; Li, X.; Zhou, J.; Wang, Z.; Wang, H.; Sessler, J. L. Diketopyrrolopyrrole-based fluorescence probes for the imaging of lysosomal $Zn^{2+}$ and identification of prostate cancer in human tissue. *Chem. Sci.* **2019**, *10*, 5699−5704.
(65) Lin, W.; Buccella, D.; Lippard, S. J. Visualization of peroxynitrite-induced changes of labile $Zn^{2+}$ in the endoplasmic reticulum with benzoresorufin-based fluorescent probes. *J. Am. Chem. Soc.* **2013**, *135*, 13512−13520.
(66) Gan, X.; Sun, P.; Li, H.; Tian, X.; Zhang, B.; Wu, J.; Tian, Y.; Zhou, H. A conveniently prepared and hypersensitized small molecular fluorescent probe: rapidly detecting free zinc ion in HepG2 cells and Arabidopsis. *Biosens. Bioelectron.* **2016**, *86*, 393−397.
(67) Tomat, E.; Nolan, E. M.; Jaworski, J.; Lippard, S. J. Organelle-specific zinc detection using zinpyr-labeled fusion proteins in live cells. *J. Am. Chem. Soc.* **2008**, *130*, 15776−15777.
(68) Singh, H.; Lee, H. W.; Heo, C. H.; Byun, J. W.; Sarkar, A. R.; Kim, H. M. A Golgi-localized two-photon probe for imaging zinc ions. *Chem. Commun.* **2015**, *51*, 12099−12102.
(69) Li, W.-h. Probes for monitoring regulated exocytosis. *Cell Calcium* **2017**, *64*, 65−71.
(70) Qin, Y.; Thomas, D.; Fontaine, C. P.; Colvin, R. A. Silencing of ZnT1 reduces $Zn^{2+}$ efflux in cultured cortical neurons. *Neurosci. Lett.* **2009**, *450*, 206−210.
(71) Li, D.; Chen, S.; Bellomo, E. A.; Tarasov, A. I.; Kaut, C.; Rutter, G. A.; Li, W.-H. Imaging dynamic insulin release using a fluorescent zinc indicator for monitoring induced exocytotic release (ZIMIR). *Proc. Natl. Acad. Sci. U. S. A.* **2011**, *108*, 21063−21068.
(72) Radford, R. J.; Chyan, W.; Lippard, S. J. Peptide-based targeting of fluorescent zinc sensors to the plasma membrane of live cells. *Chem. Sci.* **2013**, *4*, 3080−3084.
(73) Deng, F.; Liu, L.; Qiao, Q.; Huang, C.; Miao, L.; Xu, Z. A general strategy to develop cell membrane fluorescent probes with location- and target-specific fluorogenicities: a case of a $Zn^{2+}$ probe with cellular selectivity. *Chem. Commun.* **2019**, *55*, 15045−15048.
(74) Pancholi, J.; Hodson, D. J.; Jobe, K.; Rutter, G. A.; Goldup, S. M.; Watkinson, M. Biologically targeted probes for $Zn^{2+}$: a diversity oriented modular "click-$S_N$Ar-click" approach. *Chem. Sci.* **2014**, *5*, 3528−3535.
(75) Rathore, K.; Lim, C. S.; Lee, Y.; Park, H. J.; Cho, B. R. A two-photon probe for near-membrane zinc ions. *Asian J. Org. Chem.* **2014**, *3*, 1070−1073.
(76) Iyoshi, S.; Taki, M.; Yamamoto, Y. Development of a cholesterol-conjugated fluorescent sensor for site-specific detection of zinc ion at the plasma membrane. *Org. Lett.* **2011**, *13*, 4558−4561.
(77) Li, D.; Liu, L.; Li, W.-H. Genetic targeting of a small fluorescent zinc indicator to cell surface for monitoring zinc secretion. *ACS Chem. Biol.* **2015**, *10*, 1054−1063.
(78) Li, D.; Huang, Z.; Chen, S.; Hu, Z.; Li, W.-h. GLP-1 receptor mediated targeting of a fluorescent $Zn^{2+}$ sensor to beta cell surface for imaging insulin/$Zn^{2+}$ release. *Bioconjugate Chem.* **2015**, *26*, 1443−1450.
(79) Dittmer, P. J.; Miranda, J. G.; Gorski, J. A.; Palmer, A. E. Genetically encoded sensors to elucidate spatial distribution of cellular zinc. *J. Biol. Chem.* **2009**, *284*, 16289−16297.
(80) Ting, J.; Mei, F.; Mengyao, Z.; Jianwen, Q.; Hu, Z.; Yong, G. A novel cholesterol conjugated fluorescence probe for $Cu^{2+}$ detection and bioimaging in living cells. *Spectrochim. Acta, Part A* **2020**, *227*, 117530.
(81) Zhao, W.; Carreira, E. M. Conformationally restricted aza-bodipy: a highly fluorescent, stable, near-infrared-absorbing dye. *Angew. Chem., Int. Ed.* **2005**, *44*, 1677−1679.
(82) Wüstner, D. Fluorescent sterols as tools in membrane biophysics and cell biology. *Chem. Phys. Lipids* **2007**, *146*, 1−25.
(83) McCabe, M. J. Jr; Jiang, S. A.; Orrenius, S. Chelation of intracellular zinc triggers apoptosis in mature thymocytes. *Lab. Invest.* **1993**, *69*, 101−110.
(84) Rehm, D.; Weller, A. Kinetics of fluorescence quenching by electron and H-atom transfer. *Isr. J. Chem.* **1970**, *8*, 259−271.
(85) Heinrich, G.; Schoof, S.; Gusten, H. 9,10-Diphenylanthracene as fluorescence quantum yield standard. *J. Photochem.* **1974**, *3*, 315−320.
(86) Ryu, S. Y.; Huh, M.; You, Y.; Nam, W. Phosphorescent zinc probe for reversible turn-on detection with bathochromically shifted emission. *Inorg. Chem.* **2015**, *54*, 9704−9714.
(87) Sunahara, H.; Urano, Y.; Kojima, H.; Nagano, T. Design and synthesis of a library of BODIPY-based environmental polarity sensors utilizing photoinduced electron-transfer-controlled fluorescence ON/OFF switching. *J. Am. Chem. Soc.* **2007**, *129*, 5597−5604.
(88) Lu, H.; Zhang, S.; Liu, H.; Wang, Y.; Shen, Z.; Liu, C.; You, X. Experimentation and theoretic calculation of a BODIPY sensor based on photoinduced electron transfer for ions detection. *J. Phys. Chem. A* **2009**, *113*, 14081−14086.
(89) Wu, Y.; Peng, X.; Guo, B.; Fan, J.; Zhang, Z.; Wang, J.; Cui, A.; Gao, Y. Boron dipyrromethene fluorophore based fluorescence sensor for the selective imaging of Zn(II) in living cells. *Org. Biomol. Chem.* **2005**, *3*, 1387−1392.
(90) Puckett, C. A.; Barton, J. K. Mechanism of cellular uptake of a ruthenium polypyridyl complex. *Biochemistry* **2008**, *47*, 11711−11716.
(91) Li, C.; Yu, M.; Sun, Y.; Wu, Y.; Huang, C.; Li, F. A nonemissive iridium(III) complex that specifically lights-up the nuclei of living cells. *J. Am. Chem. Soc.* **2011**, *133*, 11231−11239.
(92) Hosta-Rigau, L.; Zhang, Y.; Teo, B. M.; Postma, A.; Staedler, B. Cholesterol - a biological compound as a building block in bionanotechnology. *Nanoscale* **2013**, *5*, 89−109.
(93) Mouritsen, O. G.; Zuckermann, M. J. What's so special about cholesterol? *Lipids* **2004**, *39*, 1101−1113.
(94) Komatsu, K.; Urano, Y.; Kojima, H.; Nagano, T. Development of an Iminocoumarin-based zinc sensor suitable for ratiometric fluorescence imaging of neuronal zinc. *J. Am. Chem. Soc.* **2007**, *129*, 13447−13454.


https://dx.doi.org/10.1021/acs.inorgchem.0c01376
*Inorg. Chem.* XXXX, XXX, XXX−XXX